



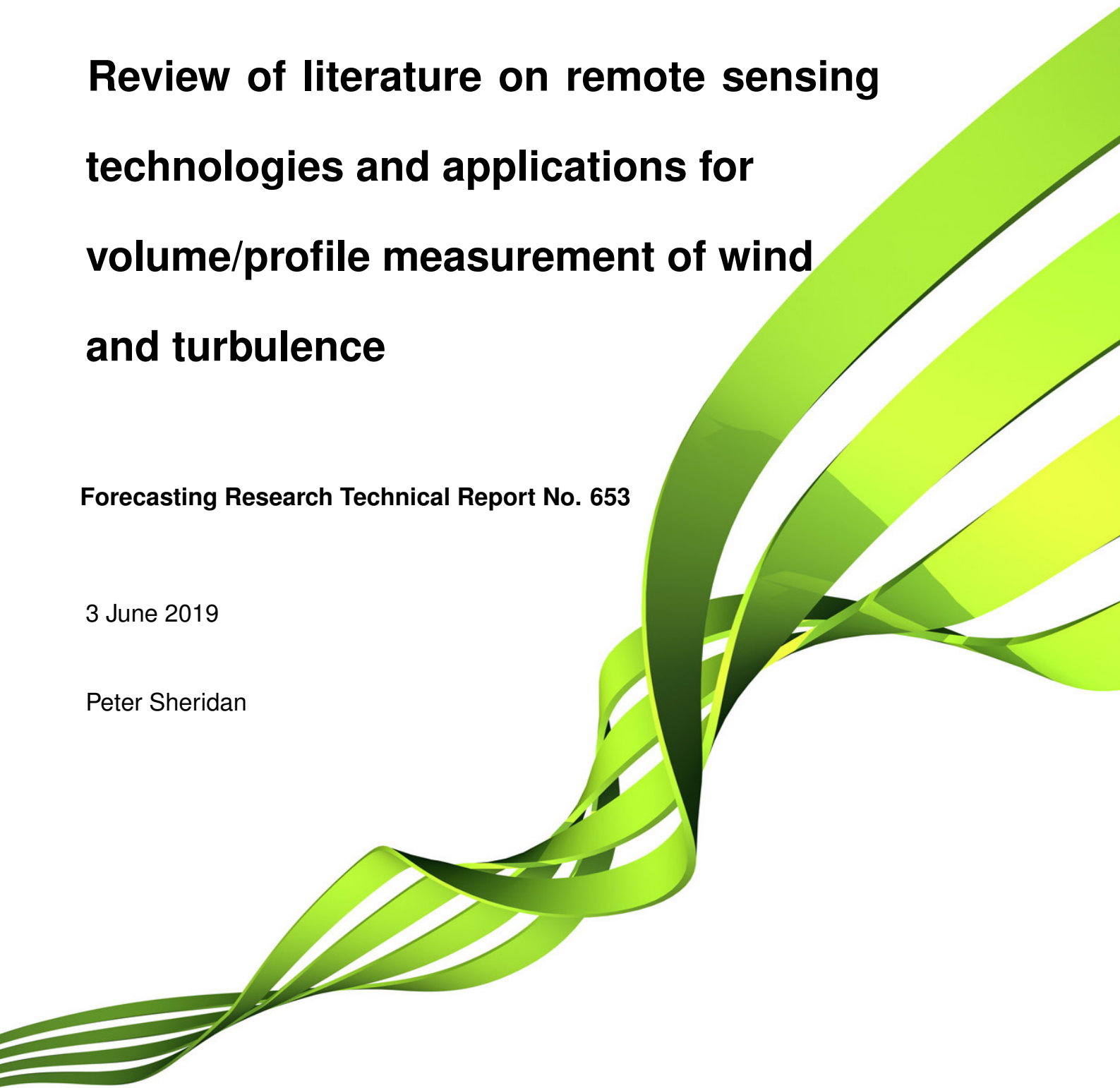
Met Office

**Review of literature on remote sensing
technologies and applications for
volume/profile measurement of wind
and turbulence**

Forecasting Research Technical Report No. 653

3 June 2019

Peter Sheridan



Abstract

This document looks at options for areal/volume and profile measurements of wind that can be used to gain a revealing insight into the microscale structure (at turbulence length scales) of complex and changing or highly turbulent flows, for forecasting/nowcasting purposes, and for comparison against spatial and temporal variation found in high resolution models, for the purposes of verification and research. The context of the review relates to a need to characterise stable flows over complex terrain involving lee waves, hydraulic jump-type flows and rotors, in particular cases which occur on a relatively small scale in the lee of comparatively modest sized mountains/hills, and the primary focus is on the lower troposphere. Principally, three remote sensing types are considered: scanning doppler lidar, scanning doppler radar, and radar wind profilers, with stronger focus on the first two. Thanks to the scale of the phenomenon in question, it could be argued that scanning doppler lidar offers the best solution as a primary instrument. Scanning doppler radars tend to be more expensive, power hungry, and have limitations in terms of the need for the appropriate (radar frequency dependent) hydrometeors to be present, though are likely to have a longer range, and operate in conditions (e.g. in-cloud) where lidar may be compromised, and can form a complementary pairing with lidar. Wind profilers are essentially unidirectional, with no areal measurement possible, but could be used as supporting instrumentation to add coverage or range to a deployment.

1 Introduction

In considering the options for a field deployment of remote sensing (and supporting measurement) equipment, it is useful to summarise the capabilities, limitations and use cases of current known remote sensing instrumentation in the literature in comparable applications. This review is not exhaustive and the starting point is around field campaigns and studies familiar to the author, who has used remote sensing data (lidar) in research work, but has no experience of operating remote sensing equipment or prior intimate knowledge of remote sensing techniques. The application in question relates to lee waves, gap flows, downslope windstorms and rotor flows in the lee of a small area of complex terrain involving a long ridge varying in height within ~ 400 m to ~ 600 m ASL, and around 10-20 km wide along its length. The review is broken down into sections regarding lidar, radar, wind profilers and studies combining more than one of these techniques together. Beam-based remote sensing techniques measure radial velocities away from the instrument and further sections cover the retrieval of wind vectors using multiple instruments or analysis techniques to retrieve this information from a single instrument using approximations. In addition, techniques for using such instruments to measure turbulence properties are discussed. The operating principles are not discussed in depth, only enough to highlight the constraints of each technique. There is more detailed reference material within some of the references quoted here but also in textbooks and documents easily obtained online.

2 Doppler wind lidar

Lidar involves partial backscattering of laser light (typically in IR: 1.5–2 μ m) from suspended particles of aerosol and water droplets (including precipitation). Cloud droplets scatter the light very strongly, however, so that only the edges of clouds are likely to be visible as the beam rapidly decays into the cloud. Aerosol is most abundant in the boundary layer (BL) and therefore, aside from clouds, beam returns are likely to be limited outside the BL. A guide by the World Meteorological Organization (2014b) briefly covers the different kinds of wind lidars available, but the general principle involves heterodyne combination of the outgoing beam and returning scatter to determine doppler shift, assuming elastic scattering of the returning photons.

Current lidar instruments are well suited to monitoring turbulence and small scale wave structures (e.g. Menke et al., 2018) or recirculations (e.g. Menke et al., 2019) in the lee of small terrain, with lidar range gate resolutions frequently O(10 m) (e.g. Menke et al., 2018). Recently, a Halo Photonics scanning doppler lidar was installed by Met Office scientists at an airfield downwind of prominent coastal headland rocks. The instrument was used during its development phase in a single angle "staring" mode to verify a CFD model which was used to build a picture of likely turbulence conditions for different wind directions and strengths at the airstrip. The instrument continues to be used in an approach path staring mode for forecast model checking by forecasters, and to give pilots an idea of the head-/tailwind and turbulence conditions to expect on approach. Similarly, Li and Chan (2016) use radial velocities in a Plan Position Indicator (PPI) azimuth-scanning mode from a lidar at Hong Kong International Airport (HKIA) to verify a CFD forecasting approach in a case of coherent eddy shedding from the adjacent mountains. Shun and Chan (2008) show examples of different flow types including gap flows, hydraulic jumps and lee waves in radial velocities from the same lidar, and how they manifest themselves in the lidar's radial wind field in PPI and RHI scans. Shun et al. (2003a) show how, in addition to intuitive interpretation of direction from the pattern of radial winds, Automatic Weather Station (AWS) data were used to confirm the direction of strongly perturbed winds within these flows, and confirm the flow type. AWS are also used to validate the radial wind detected by the lidar.

This approach of combining the lidar radial velocities from a 2D scan with ancillary, more localised wind *vector* information from supporting measurements is common. Examples include a radar wind profiler at Nice Côte d'Azur airport (Boilley and Mahfouf, 2013), AWS and dropsondes in a downslope windstorm with unsteady flow separation, during the Terrain-induced Rotor EXperiment (T-REX, Kuhnlein et al., 2013), which was bookended by and interacted with up- and down-valley flows.

Kuhnlein et al. (2013) also demonstrate how intelligent use of scanning strategies can be employed to get the most out of lidar measurements of these sorts of flows, with vertical Range Height Indicator (RHI) and horizontal PPI scans used to periodically capture the instantaneous 3D structure of the windstorm, and a staring mode used to map temporal variation of patterns and intermittency

cross-valley and in the vertical in detail.

The situation-dependent limitations of lidar range are also illustrated by Kuhnlein et al. (2013). Typically lidar range is limited to less than 10 km by atmospheric attenuation (Oude Nijhuis et al., 2018), even assuming an optimal distribution of scatterers. As already stated, though, the actual distribution of scatterers follows stratification, and figures in Kuhnlein et al. (2013) show how the shallow BL under a downslope windstorm can limit scatterer availability to a narrow near-surface band in the vertical, while dilation in a rotor flow results in the opposite, until cloud forms in ascent regions, curtailing returns.

Although Lottman et al. (2001) report lidar velocities up to and through a 1 km deep, optically thick cloud deck using a 5 Hz pulsed $2\mu\text{m}$ lidar, generally measurements within such clouds, or fog, are limited (e.g. Grund et al., 2001). Measurements in optically thin cloud and precipitation, where signal attenuation is weaker, are, however, possible (Grund et al., 2001; Koch et al., 2006; Oude Nijhuis et al., 2018). Precipitation partially contaminates measurement of vertical motion due to droplet fall speed (Lottman et al., 2001; Koch et al., 2006; Buhl et al., 2015; Traumner et al., 2008), though since lidar backscatter is proportional to the second moment of particle diameter within a measurement volume (Borque et al., 2016), this is minor compared to radar, being weighted toward smaller, sedimenting droplets. Returns from these, and the near edge of clouds above the BL can in fact enhance vertical coverage (Devara et al., 2015; Ralph et al., 1997; Grund et al., 2001; Strauss et al., 2016), as well as tracking the position of wave and rotor clouds. Oude Nijhuis et al. (2018) concisely diagram the operating range of a $1.5\mu\text{m}$ pulsed scanning doppler lidar as a function of visibility and rain rate. Unusual sources of scatterers can further enhance coverage, such as from volcanic eruptions, which can fill the entire troposphere with scatterers (e.g. Ralph and Neiman, 1997, after the Pinatubo eruption). Active volcanoes exist in significant numbers in many mountain ranges, for instance many along the length of the Andes.

Chouza et al. (2016) demonstrate the use of an airborne doppler lidar instrument to observe lee waves downwind of the tropical Cape Verde Islands. Comparisons of *in-situ* aircraft measurements of vertical velocity match well with the lidar measurements at the nearest range gate, while the lidar's ranging capability allows detection of the waves in detail over a much deeper layer.

Scan rates for lidar instruments are adjustable and vary from instrument to instrument, and the choice of scanning rate depends on the availability of scatterers, which controls signal-to-noise ratio for a given resolution, and the desired resolution, which controls the intensity of scatter from which meaningful measurements must be made for a given range gate. High resolution or less abundant scatterers requires a lower scan rate (longer dwell-time) to obtain good data quality and coverage/effective range. Traumner et al. (2008) quote $0.1\text{--}25^\circ\text{s}^{-1}$ for a WindTracer lidar, while in practice scan rates less than 10°s^{-1} seem to be common. Boilley and Mahfouf (2013) describe obtaining a PPI scan every 3 minutes using a WindTracer lidar. Adler and Kalthoff (2016) show RHI scans at 30 minute intervals, while describing a scan routine involving 2 PPI scans and 4 RHI scans per cycle which appears to occur during a 2-3 minute interruption of a vertically staring mode.

Weissmann et al. (2009) state that lidar full RHI scans using a WindTracer instrument during T-REX took 30-150 s. Menke et al. (2018) describe a strategy in which roughly 30° scans were obtained in 1 minute using short range WindScanner lidars, although this also involved synchronisation between three instruments. The Met Office-operated Halo Photonics lidar in the deployment described above performed half-RHI scans at regular intervals, taking about 90 s, focussed on obtaining high resolution (~15 m) to study small scale terrain wake flow structures.

Thobois et al. (2018) review the use of Leosphere WindCube lidars at several airports, for measuring gusts, eddies and aircraft wakes. They also review some of the literature on doppler lidar, including a review of instrument costs, performance and limitations by Steen et al. (2010). Steen et al. (2010) perform a short survey of a wide range of remote sensing instruments including lidar, radar and wind profiler instruments of different types, in relation to aviation weather and wake vortex applications at airfields.

3 Doppler radar

Scanning doppler radars operate at a much larger wavelength (lower frequency) than lidar. Returns from these radars are due to scatter mainly from hydrometeors (including cloud droplets). Weather radar operating frequencies are broken down as: S-band (2–4 GHz), C-band (4–8 GHz), X-band (typically ~9 GHz), Ka-band (~35 GHz) and W-band (~90 GHz). Ka-band is the part of the K-band “above” a water resonance peak at 22.24 GHz (another band at 12-18 GHz, Ku, “under” this peak, is more seldom used for weather applications).

S–X bands primarily scatter from precipitation, with beams attenuated (similar to lidar) in cloud. Ka and W bands primarily scatter from cloud, and are attenuated in precipitation (though returns still occur). Vertical motion detection is therefore contaminated by the fall speed of the hydrometeors for all of this type of radar (Traumner et al., 2008; Borque et al., 2016; Buhl et al., 2015; Pokharel et al., 2017), dominated in each case by droplets of smaller size (slower) with increasing radar frequency, and this must be corrected for. Especially Ka and W band radars can also be served by clear air returns, for instance as reported by Adler and Kalthoff (2016) in a moist maritime climate (Corsica) for Ka-band, Gunter et al. (2015); Hirth et al. (2017); Lundquist et al. (2017) using the mobile Texas Tech University (TTU) Ka-band radars, and more rarely using X-band radar (Oude Nijhuis et al., 2018). Barbaresco et al. (2015) interestingly indicate (using radar simulations) that turbulence in the form of aircraft wake vortices can generate sufficient radar cross section (RCS) to be detectable by X-band radar. Radar also scatters from insects within roughly 1 km of the surface, although such returns will be confined to, at most, moderate wind conditions.

W-band radars are strongly attenuated by atmospheric water vapour (Kollias et al., 2014a). The operating range of scanning doppler radars decreases with increasing frequency, with examples in the literature showing X-band radars retrieving winds up to maximum ranges of around 30–60 km (Kollias et al., 2014b; Oude Nijhuis et al., 2018; Hirth et al., 2017), Ka-band 10–30 km (Traumner

et al., 2008; Kollias et al., 2014b; Hirth et al., 2017; Moran et al., 1998) and W-band up to 20 km (Kollias et al., 2014b; French et al., 2015), although this also depends on whether or not returns are from clear air, and the size of hydrometeors or cloud droplet scatterers (Kollias et al., 2014b).

Modern Ka and W band instruments can operate with range gates of 15–30 m (Traumner et al., 2009; Kollias et al., 2014a; Buhl et al., 2015; Gunter et al., 2015; Adler and Kalthoff, 2016; Hirth et al., 2017; Lundquist et al., 2017), though actual pulse width is on the higher end of this range. X-band instruments typically have longer range gates 50–200 m (Wurman et al., 1997; Valenzuela and Kingsmill, 2018; Oude Nijhuis et al., 2018; Matrosov et al., 2005), although pulse compression can be used to give range gates as short as 5 m (Barbaresco et al., 2015; Oude Nijhuis et al., 2018). The instruments discussed by (Kollias et al., 2014a,b) are the scanning ARM cloud radars (SACR) of the U.S. Department of Energy (DOE) Atmospheric Radiation Measurement (ARM), which are dual frequency (two beam heads on the same pedestal) Ka/W and X/Ka combinations.

A new development of an X-band scanning doppler radar using high repetition frequency compressed pulses has produced an instrument that escapes some of the typical limitations of radars in this band. It can observe using 15 m range gates out to over 30 km range with good clear air returns at full range, which remain reasonable even using rapid scanning (12 s for a full 360° PPI scan), greatly outstripping the TTU Ka-band radar in this respect (Hirth et al., 2017). Pulse compression is stated by Gunter et al. (2015) as creating the ability “to combine the sensitivity achieved using a relatively long pulse without sacrificing range resolution”, and gives the TTU Ka-band radar a range resolution of 15 m. Weiss et al. (2009) further discuss technical aspects required to achieve this range resolution/sensitivity optimisation, which notably appears to increase the distance of the first range gate to 3 km from the radar. Steen et al. (2010) also separately report recently developed X-band instruments capable of good returns in clear or even, for a high power instrument “very-clear” air. They also indicate that C-band weather radar of Meteo France have been found to give 50% clear air returns up to 15 km range and 500 m altitude.

Pulse compression does not automatically result in the X-band range minimum being long, however (Barbaresco et al., 2015). The DOE operate one of the above X-band radars, and a pair are also installed on the east coast of England in a project called “beamed radar for energy assessment and site conditions” (BEACon), for dual-doppler monitoring of winds across an offshore wind power turbine field at 50 m resolution (Valdecabres et al., 2018; Nygaard and Newcombe, 2018, <https://orsted.tw/en/News/2018/05/CEO-HENPO-visit-Taiwan>, <https://nawindpower.com/texas-tech-teams-new-radar-prototype-could-help-lower-energy-costs>). Similar to the pulse-compressed TTU Ka-band radar, however, these radars are limited by a minimum range of 3 km creating a substantial coverage gap around the radar location (Hirth et al., 2017), particularly limiting for vertically pointing applications.

The range at which the first gate generally lies for different band doppler radars found in the literature are, W-band: 100–500 m (French et al., 2015; Kollias et al., 2014b; O’Connor et al., 2005), Ka-band: 100–500 m (Moran et al., 1998; Traumner et al., 2010; Kollias et al., 2014b; Hogan

et al., 2005), X-band: 100–500 m (Valenzuela and Kingsmill, 2018; Medina and Houze Jr., 2016).

Scanning can be provided by rotation of the instrument to trace a circle of range around itself, or by horizontal motion of the instrument e.g. when mounted on an aircraft (French et al., 2015). This motion, if sufficiently fast compared to the evolution of the observed phenomenon, also offers the ability to perform dual-doppler analyses (Wurman et al., 1997; French et al., 2015). Scan rates for rotating radar instruments are controlled by parameters such as pulse repeat frequency, beam width and any intentional oversampling, and tend to be $5\text{--}10^\circ\text{s}^{-1}$ for RHI scans, and $10\text{--}30^\circ\text{s}^{-1}$ for PPI scans. Slower scans are possible for better sensitivity. The Wyoming Cloud Radar (WCR) is used onboard the University of Wyoming King Air (UWKA), which travels at an airspeed of 100 ms^{-1} , so the radar's dwell time of 32 ms for a single profile scan gives a horizontal resolution of 3 m (Strauss et al., 2015), but scans will take much longer than for rotating stationary instruments for an equivalent area.

A significant issue with radar is aliasing at long ranges or large velocities, which depends on the wavelength and pulse repetition frequency. Beyond a certain range, far returns are outpaced by near returns from the next pulse, so that results are contaminated (range folding, double returns). Effective range is therefore limited by pulse repetition frequency (decreasing with increasing PRF). Similarly, since doppler velocities are determined from the difference in phase between outgoing and incoming pulses, sufficiently large velocities result in changes of phase greater than π (defined by the Nyquist velocity, a function of PRF and wavelength), and slightly larger positive velocities, for instance, cycle to the bottom of the Nyquist range to be detected as negative velocities (Bose, 2016). This is termed velocity folding and in the case of the W and Ka band radars described by Kollias et al. (2014a,b), is equal to 4 ms^{-1} and 10.6 ms^{-1} , respectively. Increasing PRF increases the Nyquist velocity but also decreases maximum range, so there is a trade-off. A process of unfolding using velocity continuity and reference information such as a sounding is necessary to retrieve actual velocities (Kollias et al., 2014b; Bose, 2016). Numerous algorithms exist to perform this process reliably (<https://www.nssl.noaa.gov/publications/dopplerguide/chapter1.php>).

Doppler radars vary greatly in size and power consumption, but effective models can be fairly manageable in size, e.g. the X-band scanning radar discussed by Oude Nijhuis et al. (2018) or the Ka-band radar used by Adler and Kalthoff (2016), pictured in Figure 3 of Ducrocq et al. (2014).

The spatial resolution, speed, range versatility and ability to obtain measurements in cloud and/or precipitation of scanning doppler radars makes such instruments of one sort or another suitable for detailed 2D or 3D measurement of a variety of phenomena including trapped waves (Koch et al., 2008; Strauss et al., 2015, 2016; French et al., 2015), downslope winds and hydraulic jumps (Strauss et al., 2015; French et al., 2015; Pokharel et al., 2017), rotors (French et al., 2015; Pokharel et al., 2017; Strauss et al., 2015), tornadoes (Weiss et al., 2009), Kelvin-Helmholz waves (Medina and Houze Jr., 2016), orographic wakes and wake vortices (Shun et al., 2003b; Chan and Hon, 2016) and turbine and aircraft wakes (Valdecabres et al., 2018; Nygaard and Newcombe, 2018; Oude Nijhuis et al., 2018; Barbaresco et al., 2015). Particularly nice examples involving cloud

radar, relevant to the present application, can be seen in papers of Strauss et al. (2015); French et al. (2015); Pokharel et al. (2017), clearly depicting the structure of wave/jump features, but show how coverage is limited by the reliance on the presence of water droplets. Only part of the flow may generally be mapped, but the shape of clouds present (in the case of cloud radar) is captured, which helps to build a picture of the flow structure.

4 Wind profilers

SODAR is an acoustic vertical wind profiling technique. Primarily aimed at boundary layer study, limitations such as its short range (~ 100 s of metres), contamination and signal loss in high winds, reduced performance in the presence of temperature inversions (which frequently accompany strong lee wave cases), and limitations in noisy environments make SODAR relatively unsuitable for airport deployment in the study of lee wave activity. Therefore this section focusses on radar wind profilers (but see Kadygrov, 2005; Chan, 2008; World Meteorological Organization, 2014b, for further information).

Doppler radar wind profilers are most commonly UHF instruments which generally use a doppler beam swinging technique (DBS, vertical and say $4 \times 15^\circ$ off-vertical single path scans which can be combined to obtain all 3 wind components), capable of measuring winds roughly up to the tropopause, depending on conditions, frequency and transmitter power (World Meteorological Organization, 2014b). Using spaced antennae instead of DBS allows faster wind measurement, since all required directional samples may be taken simultaneously (Cohn et al., 2011). UHF profilers do not require hydrometeors to obtain returns, operating primarily using Bragg scattering from density fluctuations, and eddies moving with the mean flow. Some Rayleigh scattering from particles (including water droplets) may occur, however, producing a small downward bias in the measured wind (Buhl et al., 2015). Troposphere profilers with frequencies ~ 400 MHz are attenuated slightly in light rain, while boundary layer profilers (~ 1000 MHz) are attenuated strongly by precipitation (World Meteorological Organization, 2014b). Minimum ranges depend on measurement mode (see below).

Duration of a single full 3D wind profile measurement varies and can be as short as 10 s for large, powerful instruments (Buhl et al., 2015), but are more often up to 30 minutes (Cohn et al., 2011; Drechsel et al., 2009; Udina et al., 2017) for smaller single antenna instruments, taking into account averaging of multiple repeat scans required to obtain stable data. Vertical velocity information alone can, however, be determined more frequently at the expense of the 3D wind information (Cohn et al., 2011). Boilley and Mahfouf (2013), meanwhile, describe a BL wind profiler operating at 1274MHz which obtained profiles every 2 minutes at Nice Cote d'Azur airport, either between 75 m and 2000 m up at 75 m resolution, or between 300 m and 5000 m at 150 m resolution (these dual range options are common for UHF wind profilers, involving changing pulse width). Profiler resolution is commonly in this range (Buhl et al., 2015; Cohn et al., 2011; Drechsel et al., 2009; Paschke et al.,

2015; Valenzuela and Kingsmill, 2017), while the lowest gate is more usually around 500 m (Buhl et al., 2015; Cohn et al., 2011; Paschke et al., 2015; Drechsel et al., 2009). Lundquist et al. (2017) quote resolution of 25 m, meanwhile (while also discussing fast measurements at 2 minute intervals) with the lowest gate shown at 100 m for a 915MHz profiler; Valenzuela and Kingsmill (2017) state a lowest gate at 150 m for the same beam frequency (producing measurements at 1 minute intervals).

A notable use case of boundary layer wind profilers for airfield safety is their incorporation into the Juneau Airport Wind System (JAWS), at an airport surrounded by mountainous terrain in Alaska. This includes a terrain-induced turbulence alert system in which data from three closely spaced wind profilers around the airport are used. A “rapid update” mode is employed, instead of the normal long averaging period, with data taken every 30 s (enabled by proprietary data quality algorithms to improve reliability; statistics are also improved by combining data from multiple levels) along with anemometer data from the surrounding terrain and aircraft onboard data as input to a regression model for turbulence detection and warning (Politovich et al., 2011).

Middle and Upper (MU), or Stratosphere Troposphere, radar profilers, which are very large instruments operating at very high power in the VHF frequency band (~ 45 MHz) again have the advantage of performing well regardless of the presence or otherwise of precipitation or cloud, but operate up to much greater heights than UHF (World Meteorological Organization, 2014b). An instrument located at Aberystwyth has a vertical resolution of 150 m with the first range gate at ~ 2000 m, and acquires profiles of the 3D wind vector every 95s (Worthington, 1998; Lawson et al., 2011). A newer instrument is located near Shigaraki in Japan, with a similar resolution but a lower first range gate at about 500 m, and much faster sampling, completing a profile every 6.55s (Worthington, 2004). VHF radar reflections from stable layers can be exploited to study gravity wave motion and crest orientation since wave-induced tilting of these layers creates stronger returns for off-zenith scan directions, whereas normally the strongest returns come from directly vertical beam pointing (Worthington, 2005). This is possible due to the beam-steering capability of the radar, which is normally used for DBS to obtain 3D wind vectors. This beam swinging capability (within a range $\sim 30^\circ$) has also been used to obtain 3D measurements of convective systems in a volume over the radar (Worthington, 2004).

Wind profilers’ long (and adjustable) range and relative insensitivity to operating conditions see them used in a very wide variety of research and operational roles. VHF (Worthington, 1998; Vosper and Worthington, 2002; Worthington, 2005) and UHF (Cohn et al., 2011; French et al., 2015; Strauss et al., 2016; Udina et al., 2017) profilers have been used to study the broad motion present in or upwind of mountain wave, rotor and downslope windstorm events, though their (generally) comparatively poor resolution and near-instrument coverage, and especially their (generally) slow update time usually put them in a supporting role to faster and more flexible instruments such as lidar or radar where available (Strauss et al., 2016). The VHF radar at Shigaraki has also been used to study travelling Kelvin-Helmholz rolls (Luce et al., 2018). A fast, high resolution 915MHz wind profiler has been used for boundary layer turbulence study (Lundquist et al., 2017), using doppler

spectra to obtain turbulence information for finely spaced (25 m) range gates.

5 Use of combined techniques

Frequently, two or more remote sensing instruments are used in tandem, taking advantage of complementarity between two different kinds of instrument. Alternatively, supporting, in situ measurements or wind profilers can be used to verify (Strauss et al., 2015; Chouza et al., 2016) or to augment the usefulness of a scanning remote sensing instrument by resolving the inevitable ambiguities that arise from radial velocity providing only one wind component at a given location, as already described in section 2 (Shun et al., 2003a; Boilley and Mahfouf, 2013; Kuhnlein et al., 2013), or providing upwind information as described in section 4 (French et al., 2015; Udina et al., 2017).

Strauss et al. (2016) describe a tour de force of multi-instrument synthesis of this kind for T-REX IOPs, using google earth to combine lidar RHI and PPI scans and multiple wind profilers and AWS (giving vector information), all located in the same area, for one case. They examine a further case using RHI and PPI lidar scans augmented again by a dense AWS network affording vector information, and combining Ka-band airborne radar data with in-situ aircraft data in stacked legs out-of-cloud to build up further vertical cross-sections through the windstorm flow.

Radar/lidar combinations are fairly common. For instance, Traumner et al. (2008, 2009); Adler and Kalthoff (2016); Borque et al. (2016) compare lidar and Ka-band radar in vertically pointing mode, the latter two studies showing Hovmoeller-style timeseries of the vertical velocity profile overhead in different conditions. Both show the complementarity of the two instruments, with each able to detect where the other may not, depending on the conditions, but with a degree of overlap where the two techniques can be used to reinforce each other's results or detect differences for instance due to hydrometeor fall speed affecting radar more strongly, and thus improve the overall information available. Adler and Kalthoff (2016) in fact show deeper coverage for the radar than for the lidar in Corsica, providing information below cloud base. Traumner et al. (2009) demonstrate cases where a complete vertical profile is available, but originates from only one of the two instruments (radar or lidar), or is composited in distinct, exclusive zones from both, emphasising this complementarity and characterising the balance of coverage between the two instruments in terms of cloud cover, precipitation and humidity. Other examples include the doppler weather radar and doppler lidars deployed at HKIA (Hon and Chan, 2014), and radar/lidar at Las Vegas International Airport (Keohan et al., 2006, highlight the complementary conditions that are optimal for each of the two techniques). Both of the latter airports are surrounded by sizeable hills or mountains. Steen et al. (2010) also emphasise the complementary pairing of radar and lidar to accommodate the range of possible weather situations.

Oude Nijhuis et al. (2018) combine scanning lidar and (X-band) radar, in a PPI configuration, for the Ultrafast Wind Sensors (UFO) project at Toulouse-Blagnac airport, also adding X-band and lidar vertical profilers and Mode-S downlinks (see later) to the inventory. Lidar and radar PPI data are

effectively composited, with lidar used in the nearest 5 km, and radar used outside this to a range of nearly 30 km (though in ‘near mode’, the radar can scan at 5 m resolution at up to 2 km range Barbaresco et al., 2015); the radar is intended to accommodate times when the lidar is attenuated by rain. Model improvements accompany the project, including assimilation of the lidar profiler and Mode-S data into a 1 km resolution model, which yields benefits especially at short lead times (~ 1 hr), though upwind measurements are expected to yield greater benefits.

Koch et al. (2008) demonstrate the use of doppler S-band radar PPI and RHI scans, vertically pointing doppler lidar, airborne aerosol lidar and regional surface measurement network analysis to build a comprehensive picture of a travelling bore and its origins. Similarly, Luce et al. (2018) combine data from the Shiguraki VHF radar, micropulse and Raman lidars, all vertically pointing, and cloud images from a fish-eye lens all-sky camera to characterise a sequence of breaking Kelvin-Helmholz waves, utilising their travel overhead to obtain a time-height cross-section. In both of these papers, each instrument measures a different quantity, and thus a ‘layered’ view of the influence of the same dynamical object on its environment is presented.

The Perdigao campaign, measuring flow over two modest, parallel ridges in Portugal was remarkable for utilising 32 lidar instruments simultaneously, enabling multiple-instrument scanning strategies for increased coverage and to measure different wind components at the same point (Fernando et al., 2019). The use of dual or multiple remote sensing instruments observing a point from different directions to obtain wind vector information is discussed in the next section.

Although Steen et al. (2010) describe doppler radars capable of obtaining good returns from clear air, they suggest a cost-optimal combination of lidar for clear air and X-band radar for conditions of precipitation, the combination used by Oude Nijhuis et al. (2018).

6 Wind vector retrieval

Instead of relying upon independent measurements such as surface AWS or profilers to provide wind vector information to help interpret wind patterns in PPI or RHI scans from scanning instruments, a number of methods exist to retrieve vector information from the radar/lidar data itself. Perhaps the simplest method is DBS, described above in section 4, which produces a 3D vector wind profile representing a narrow cone above the instrument. An analogous method available to scanning instruments is the Velocity Azimuth Display (VAD) technique. This involves the calculation of a wind vector profile representative of the area of a PPI scan by assuming a horizontally homogeneous wind vector at a given range (equivalently height for a conical scan) so that a sine wave may be fitted to the radial wind data at that range to obtain the magnitude of the vector. This method becomes compromised when the assumption of horizontal homogeneity is significantly violated, such as in a vigorous convective boundary layer, or due to other large amplitude small scale variations, including rotors and potentially lee waves depending on their amplitude and wavelength. Banakh and Smalikho (2016) use VAD profiles to study travelling gravity wave structures at Lake

Baikal, while Witschas et al. (2017) use VAD-style profiles of the 3-D wind vector from an airborne lidar to provide in effect a “scanning profiler”, albeit at 9 km horizontal resolution due to a scan time of 21 minutes.

A common example of more sophisticated vector retrieval involves the use of two or more (dual- or multiple-doppler) instruments scanning the same area or on intersecting planes. This removes ambiguity that would exist in the radial velocity for just one instrument since trigonometry can be used to retrieve a 2-D or 3-D vector (depending on the number of instruments and their positioning). This requires a degree of synchronisation, however, since measurements at the same point at different times will not be measuring the same air parcel. Due to the spreading distribution and increasing size of the “fan” of data cells with increasing range in a radial scan, and the finite time to complete a scan, perfect synchronisation of all cells in a plane, even for instruments of the same model running the same scan sequence, is not possible. Intersections along a line can, meanwhile, be synchronised. Cells will also not match perfectly in volume, and in conical (PPI) scans, the measurement cones of the instruments will not coincide perfectly in most areas. In practice typically some tolerance is placed on the time and space separation of cells combined from separate instruments, and sampling onto a regular grid is used to homogenise measurement volumes.

Drechsel et al. (2009) used the Multiple Doppler Synthesis and Continuity Adjustment Technique (MUSCAT) algorithm for dual-doppler analysis of lidar data from two similar models of scanning instrument from the T-REX experiment, each with 100 m range gate resolution. This involves building a 3-D radial wind map using multiple (12) stacked PPI scans for each instrument. MUSCAT combines the information from the separate lidars with the continuity equation to obtain 3-D wind vectors on a regular grid, in this case cubic with 200 m resolution. A Cressman distance-weighted interpolation of the data onto the grid is used, with a 500 m radius of influence in the vertical and 1000 m radius in the horizontal. A cost function is minimised for each horizontal grid surface which involves terms representing a least squares fit of the 3-D vector components to the interpolated radial wind measurements at each grid point, a term connecting each grid surface through continuity, and a low pass filter (with a 4 grid-length cut-off), remedying ill-conditioned cells by effectively extrapolating from surrounding cells. The time taken to execute this technique and the coarseness of resolution due to the large radii of influence required to interpolate the data potentially limit its suitability for rapidly evolving, unsteady flows such as small scale rotors. However, modern instruments may have order of magnitude higher range resolution, and sacrifice of range (through decreased signal/noise from faster scans) could allow the technique to be performed fairly rapidly over a smaller volume. Notably, Barthelmie and Pryor (2019), during the Perdigao campaign, obtain relatively dense scans (compared to the above) of a 3-D volume within a small solid angle zone, also incorporating several VAD scans, within 10 minutes.

van Dooren et al. (2016) describe the Multiple-Lidar Wind Field Evaluation Algorithm (MuLiWEA) method, which is broadly a 2-D analogy of MUSCAT, but using a simpler, 2-D application of con-

tinuity in-plane for low-angle PPI scans, assuming incompressible flow. The vertical wind, w , is neglected; for low angle scans near the surface this is a reasonable assumption, in relatively flat terrain (in principle a modified method could be developed, instead assuming terrain-following flow). Simulated tests using single and stacked PPI scans in a high resolution large eddy simulation (LES) showed better error performance of the latter, but acceptable performance in the former, even in the case of vertical offsets of 15 m from the retrieval plane at 61 m AGL. Estimated errors were $O(10\%)$ on wind speed, 15° on wind direction. Real tests using lidars with 40 m range gates, using a radius of influence of 30 m had estimated errors of 5% of the retrieved wind speeds. This technique allows much more rapid, albeit 2-D planar, retrievals than 3-D MUSCAT. In both cases, synchronisation is not a strong consideration, but better approximate synchronisation will clearly reduce errors.

Choukulkar et al. (2017) describe a five-lidar (differing instrument models) volume-scanning technique that combines multiple narrow-sector PPIs from each lidar to obtain horizontal wind vectors on a 3-D grid of $15\text{ m} \times 30\text{ m} \times 30\text{ m}$ cells, but with a 5 minute time tolerance. Performance of the technique was found to be similar (though measurements much less frequent) to uncoordinated lidar virtual towers (see below).

Hill et al. (2010) utilise the same two T-REX lidars used by Drechsel et al. (2009), but this time in a vertically co-planar RHI scanning mode (roughly along-wind, cross-valley). After regridding and averaging the data within a temporal tolerance of 50 s (the instruments are not explicitly synchronised) onto a $130\text{ m} \times 130\text{ m}$ grid (optimised trade off for acceptable sampling), a relatively simple least-squares trigonometric method is used to combine the data from the two instruments to derive the 2-D in-plane wind vector for each grid cell. The data are used to depict and identify large ($\sim 1.5\text{ km}$) rotor and smaller ($\sim 400\text{ m}$) sub-rotor vortices in different cases by computing vorticity, streamlines and “swirl”. Again with more modern instruments this would be possible on a finer grid.

Several studies from the Perdigao campaign use low-angle, overlapping co-planar RHI scanning strategies to essentially circumvent the need for 2-D vector retrieval (Mann et al., 2018; Fernando et al., 2019; Menke et al., 2019). These studies use for instance RHI scans over a narrow range of angles near the horizontal, pointing across a valley towards each other from two lidars on adjacent ridge tops, so that the line-of-sight (LOS) radial velocities from each lidar closely approximate the horizontal in-plane wind component. Mann et al. (2018) use four lidars in this way, extending the picture upwind and downwind of the ridge pair. In this way, Mann et al. (2018); Fernando et al. (2019) illustrate wave-like structures in flow over the double-ridge and Menke et al. (2019) show a recirculation zone (akin to a rotor but with flow separation induced by terrain steepness rather than wave activity) in the valley. Dual-doppler near-horizontal quasi-synchronised co-planar cross-sections from two lidars on the same ridge are also shown mapping 2-D wind vectors across a wind-turbine wake on the opposite ridge by Vasiljevic et al. (2017); Menke et al. (2018).

Lundquist et al. (2017) show data from dual-doppler wind vector retrievals in a horizontal plane using the TTU Ka band radars recorded during the eXperimental Planetary boundary layer Instrumentation Assessment (XPIA), carried out at the Boulder Atmospheric Observatory (BAO). The

BEACon X-band radar pair deployed on the east coast of England also use a synchronised dual-doppler retrieval using volume-scanning stacked PPI scans to construct horizontal wind maps at wind turbine hub height in clear air or precipitation to a range of ~ 30 km on a regular 50 m grid with a temporal resolution of roughly 1 minute.

Non-coplanar intersections of two RHI scan planes can be used to construct a “virtual tower” (VT), giving a profile of wind vectors in the vertical. As with other multi-instrument techniques some spatiotemporal tolerance needs to be applied for measurements representing a given point. Pauscher et al. (2016) show the superiority of this technique to DBS by comparison to sonic anemometers, particularly when studying wind perturbations. Wang et al. (2016) used a triple lidar set-up involving two different kinds of lidar, during the Mountain Terrain Atmospheric Modeling and Observations (MATERHORN) program to obtain virtual towers via a direct geometrical relationship, using manual (imperfect) synchronisation with 2 m spatial and 5 s temporal tolerance. Bell et al. (2019) show results from numerous virtual towers of 2-D and 3-D wind vectors, constructed from Perdigao doppler lidar measurements which were not strictly synchronised, with spatial tolerance of 10 m and temporal tolerance of 60 s (justified by the relatively steady nocturnal flows being studied).

Choukulkar et al. (2017) and Debnath et al. (2017) describe triple-lidar and dual-Ka-band radar virtual towers of 3-D and 2-D wind vectors, respectively, created by coordinated scanning, and also constructed from uncoordinated RHI scans. The latter use a 15 s temporal tolerance, obtaining VTs every 15 s at 10 m vertical intervals, compared to 3 minutes required for the former, at 100 m vertical intervals (Choukulkar et al., 2017). In addition, dual-Ka-band radar virtual towers of 2-D wind vectors were constructed using the TTU instruments Debnath et al. (2017). Good performance of the coordinated lidar VTs and reasonable performance of uncoordinated lidar VTs and the radar VTs was found. Gunter et al. (2015), during XPIA, similarly used the TTU Ka-band radars for coordinated VTs, obtaining 2.5 s repetition time in a shallow (6° or 200 m) scanning configuration with data every 10 m in the vertical, and 9 s repetition time in a deeper (45°) configuration. Performance compared to sonic and propeller anemometers was found to be reasonable.

Returning to Perdigao, flexibly programmable beam control has permitted ridge-following (instead of vertical) analogues of VTs. Two or more lidars scan in a coordinated fashion with their beams intersecting at consecutive points at a fixed height directly above a ridge top (Vasiljevic et al., 2017; Mann et al., 2018), so that ridge overflow and variations along the ridge can be precisely monitored.

In principle, two different lidar or two different radar instruments, with different range gate characteristics and scan speeds can be used to perform dual-doppler analyses (Drechsel et al., 2009; van Dooren et al., 2016; Choukulkar et al., 2017). It is conceivable that instruments of different kinds (lidar and radar) could be used together in the same way. While this would introduce errors and limit coverage due to the different response characteristics of each instrument (for instance different hydrometeor sensitivities), these may be acceptable balanced against the ability to obtain wind vector information over an extensive volume, area or profile. In some conditions, the differences in

response may in fact be relatively small. This was carried out by Chan and Shao (2007) using an extension of their variational method (see below) to combine information from a lidar and S-band weather radar to obtain horizontal wind vectors from PPI scans.

Instead of using multiple instruments to obtain vector information, analysis techniques using physically-based assumptions and approximations can be employed in order to infer the corresponding wind vectors which are consistent with the radial velocity measurements within a PPI or RHI scan. One method used by Chan and Shao (2007) involves a variational approach, in which a cost function is minimised to obtain a best approximation to the real distribution of speed and direction within the scan. The function consists of six terms representing (i) deviation from a background (the background is determined via an expansion in terms of Legendre polynomials which are defined by performing the overall analysis in the absence of the deviation term), (ii) the deviation of the radial velocity reconstructed using the retrieval method from the actual measured radial velocity, (iii)-(v) smoothing terms applied to the velocity and its 2-D derivatives, and (vi) a conservation constraint. In a previous study applied to radar, this represented the conservation of precipitation content (Qiu et al., 2006), while Chan and Shao (2007) in order to apply to lidar, use conservation of the radial velocity across three consecutive scans, enforcing self-consistency of advective motion of wind structures over time. Tang et al. (2011) use the same method. Chan and Shao (2007) obtain convincing wind cross-sections of wind speed and direction modulation by lee waves, convergent flows and gap flows. Verification at an anemometer location reveals a good correspondence.

An alternative retrieval technique, Optimal Interpolation (OI) is used by Choukulkar et al. (2012, 2017), with data from the T-REX and XPIA campaigns, respectively, motivated by the rapidity of the technique compared to variational methods. This involves modifying a “background” wind field (here determined using a simple VAD scan) with an analysis increment given as a tangential/radial component vector. The increment is determined by minimising a cost function involving background and observational error covariance (several papers that Choukulkar et al., 2012, reference constitute the basis for the method). Retrievals using simulated lidar data from a very high resolution NWP model show good morphological representation of the original flow by the retrieved vectors, though with some quantitative differences (Choukulkar et al., 2012), while other comparisons with anemometer data show correspondence approaching that obtained by uncoordinated dual-doppler VTs (Choukulkar et al., 2017).

Oude Nijhuis et al. (2018) employ retrieval techniques to obtain PPI vector fields from doppler lidar and X-band radar instruments separately, using a Volume Velocity Processing (VVP) technique for lidar, but finding that an optimal estimation-based 4DVAR technique performs better for the radar. (Choukulkar et al., 2012) also refer to studies using 4DVAR for single-lidar vector retrievals.

Weissmann et al. (2009) apply a comparatively simple technique to retrieve vector information from single lidar RHI scans during rotor events in the T-REX campaign. The method works by assuming continuity applies in-plane in polar coordinates, and iterates from the surface to zenith from first one side and then the other side of a $\sim 180^\circ$ RHI scan, assuming vertical velocity is zero at the

surface. This is then smoothed along-beam to account for small-scale out-of-plane divergence and numerical errors, and a correction for large scale divergence is applied by averaging the two zenith results from each side of the RHI scan (which will be slightly different), and relaxing this correction linearly to zero back through the scan angles back to the surface. Out-of-plane divergence is probably the largest source of error. However, the authors suggest that while this impacts velocities, the vorticity, which they use to characterise rotor and sub-rotor activity, is less sensitive. The retrieved vorticity corresponds well with the character of that derived from high resolution LES for the same case.

It is also possible to retrieve 3D wind vector information at micro scales (turbulence) using rapid timelapse of volume scans from scanning aerosol backscatter LIDAR, which is significantly cheaper than a scanning doppler instrument. Four retrieval methods are discussed by (Howard Jr. and Naini, 2012).

7 Turbulence information retrieval

Turbulence can be quantified in a number of ways, for instance the simple statistical variability of the wind vector (or of a given wind component), σ , turbulence intensity, σ/U (where U is the magnitude of the mean wind, or the mean of the wind component in question), or turbulent kinetic energy (TKE), $1/2(\overline{u'^2} + \overline{v'^2} + \overline{w'^2})$, where for instance u' represents a perturbation of the westerly wind component relative to a representative mean (i.e. σ_u). An example of a simpler analysis is applied by Barkwith and Collier (2011) to lidar measurements of turbulent structures in the boundary layer, involving simply performing a VAD from a PPI scan and subtracting this from the PPI data to obtain a 'perturbation' radial velocity map. Recent literature highlights another measure, the eddy dissipation rate (EDR), ϵ . This is considered a more useful turbulence metric in aviation applications, which can be related to aircraft-specific loads and thus calibrated to individual airframes, is the International Civil Aviation Organization (ICAO, 2001) standard, and conveniently provides values between 0 and 1 (Sharman and Pearson, 2017). EDR represents the rate of viscous dissipation of turbulent energy as it cascades to sufficiently small eddy scales. The cube-root, $\epsilon^{1/3}$ is also often referred to interchangeably with ϵ as "EDR" (e.g. Sharman et al., 2014; Oude Nijhuis et al., 2018). From Kolmogorov theory, $E(k)$, the turbulent energy spectrum as a function of wavenumber, $k = 2\pi/\lambda$, with λ representing a particular eddy scale, can be obtained as,

$$E(k) = C\epsilon^{2/3}k^{5/3} \quad (1)$$

where C is a universal constant (0.55 for one-dimensional spectra). Thus one way of determining ϵ is from fits to turbulence spectra (e.g. as discussed by O'Connor et al., 2010; Krishnamurthy et al., 2011). Using Taylor's "frozen turbulence" hypothesis, in the appropriate conditions, turbulence diagnosis can be applied to temporal or spatial variations of the wind, allowing flexibility concerning

the use of measurements confined to a point, line or small area over a time period (relying on advection of turbulence through the measured space), or alternatively measurements over a large area instantaneously or over a short or period of time (the substitution $t = s/U$ can be made, where t is time, s is distance and U the mean flow speed).

Other methods exist for determining EDR, for instance via the determination of structure functions describing the spatial structure of variability within doppler instrument stares or azimuthal scans and depend on the intensity and spatial scale of fluctuations that they contain (Krishnamurthy et al., 2011). A turbulence model can be fitted to the structure function and used to back out the EDR (Krishnamurthy et al., 2011).

Another method involves assuming that the velocity variance in a range gate within sequence of stare measurements is dominated by turbulence, so that the velocity variance is equivalent to the TKE. Integrating the turbulent energy spectrum between two scales, one defined by the advection through the gate scattering volume in the duration of one stare, and the second defined by the advection that may take place during the whole sequence of stares, is then equal to the velocity variance over the sequence of stares. Assuming that both length scales are within the inertial subrange described by equation 1, then its integration between limits defined by the two length scales can be rearranged to obtain an estimate of EDR, without the need for spectral analysis (O'Connor et al., 2010; Oude Nijhuis et al., 2018). On the other hand, spectra do allow the above assumptions to be checked. We will term this the spectral integration method.

Finally, EDR can also be determined from the doppler spectral width, i.e. the spread of velocities returned from a single scattering volume (range gate), allowing much more rapid and temporally resolved EDR determination. However, while turbulence may be a dominant term in the spectral width, other factors such as beam broadening contaminate the retrieval, which may be corrected for (Oude Nijhuis et al., 2018). (Borque et al., 2016) review other terms, including due to shear, hydrometeor terminal velocity spread, cross-wind and antenna rotation for a Ka-band radar. Of these, they introduce corrections for shear, cross-wind and (crudely, for large droplets) hydrometeor spread. In simulated tests of sensitivity, they find that hydrometeor spread is only a small influence on retrieved EDR for cloud retrievals in conditions with a reasonable amount of turbulence, and that its influence in light drizzle may also not be great. In case studies, however, comparisons of radar doppler spectral width-based EDR values with spectral integration-based EDR values from lidar and radar at cloud base indicate that in a case with stronger drizzle, the contributions to spectral width from hydrometeor spread and turbulence became comparable. In a precipitating case, the hydrometeor term dominated the spectral width. Oude Nijhuis et al. (2018), meanwhile, simply confined retrievals from X-band radar data to clear air conditions.

In the studies already discussed in earlier sections, Krishnamurthy et al. (2011) use the lidar structure function approach to study turbulence in flows from T-REX, showing good correspondence with EDR determined using the spectral fitting method from tower sonic anemometer measurements. Oude Nijhuis et al. (2018) use the doppler spectral width method with an X-band radar

vertical profiler, and the spectral integration method for a scanning lidar and X-band radar (the method they use for a profiling lidar is not discussed). Hydrometeor fall speed effects on EDR values from the spectral integration method are avoided by using a large effective sampling scale for velocity variance calculation and applying the method only for low elevation PPI scans. With the doppler spectral width method, using EDR retrievals from LES-simulated radar data, they show that for low EDR values, errors in retrieved EDR grow as the Bragg scale responsible for radar scattering passes into the dissipative range, and out of the inertial subrange. O'Connor et al. (2010) use the spectral integration method with doppler lidar data. Borque et al. (2016) use a modified spectral integration technique with lidar and cloud radar data, where the inertial range integral is determined explicitly, rather than relying on approximation via velocity variance, and also test the spectral width method with radar data. Bouniol et al. (2003) use the spectral integral method, successfully validating it by comparison with the spectral fitting method. Hon and Chan (2013) use an azimuthal structure function approach and incorporate it into a skilful low-level turbulence and windshear alerting method. EDR values from this method compared reasonably well with values determined from aircraft onboard Quick Access Recorder (QAR) data. Banakh et al. (2017) perform an error analysis of the lidar azimuthal structure function method, finding significant dependence on lidar signal-to-noise ratio and the magnitude of the EDR itself.

Strauss et al. (2015) use airborne Ka-band dual-doppler radar velocity data to estimate EDR for each wind component via the spectral integral method, but similarly to Borque et al. (2016) involving explicit integration, over the carefully determined limits of the inertial subrange from computed spectra. These component estimates broadly agree but show a small degree of scatter, and a "log-mean" is applied to combine the three. The log-mean values agree well with aircraft in-situ measurements (the EDR is related to vertical accelerations experienced by the aircraft) during rotor/wave breaking events in the lee of the Medicine Bow mountains. The authors show very strong correspondence between the EDR and vertical velocity variance in low level turbulence on flights mapping vertical plane transects through the wave and rotor flow, with greatly elevated values in the rotor region, especially close to the flow separation point, and in an upper wave breaking region. Errors due to turbulence anisotropy at low EDR (stable upwind flow) are highlighted, and relative uncertainty estimation of vertical velocity variance is carried out, taking into account hydrometeor spread, and errors related to aircraft control and motion, and sampling volume, with only areas where relative uncertainty $< 25\%$ discussed quantitatively. These areas are confined to the regions of elevated values already mentioned. In a reference case with no waves, turbulence is weaker and more evenly spread within the boundary layer, with larger EDR values confined near slopes whose steepness makes flow separation likely by default.

EDR determination from doppler spectral widths is normally applied to radar, as above. Strauss et al. (2016), meanwhile, use scanning doppler lidar to examine turbulence. Instead of estimating EDR, they use lidar doppler spectral width within RHI scans as a proxy for turbulence intensity, finding that it highlights turbulent instabilities associated with shear between the edge of rotor areas

and the overlying separated flow during T-REX IOPs.

Tang et al. (2011) track coherent structures in the flow which may adversely affect aircraft, such as velocity anomalies (effectively, eddies), shed from ridges upwind on an airfield. Their method is to use the finite-time Lyapunov exponent (FTLE). This field is computed from deformations in the flow over time, and areas of large values delineate Lagrangian (advecting with the flow) coherent structures (LCS). LCS may attract or repel nearby fluid trajectories, creating local entangling or spreading of flow structure respectively. Attracting and repelling structures emerge in FTLE analysis of forward and backward time trajectories, respectively. The methodology used by Tang et al. (2011) incorporates an extension which allows easier computation of the exponents within a small domain, termed finite-domain FTLE (FDFTLE). This is applied to 2-D velocity vector retrievals obtained from single-lidar PPI scans using the variational method of Chan and Shao (2007). By a gradient analysis of the FDFTLE field to determine FDFTLE 'ridges', in effect the method allows tracking of turbulent structures approaching HKIA. Evidence of correspondence between tracked LCS and the timing of disturbances recorded onboard landing aircraft was shown.

Windshear refers to the experience of sudden cross-winds, which may compromise aircraft control, or sudden changes in headwind which cause dangerous loss of lift. Windshear and turbulence tend to be closely associated since strong shear often induces turbulence, while the velocity variation associated with turbulence implies sharp gradients of wind. Shun and Chan (2008) discuss the Lidar Windshear Alerting System (LIWAS) operated at HKIA. This involves scanning the lidar beam obliquely along the approach and takeoff paths to monitor, and warn pilots concerning, changes in head-/tail-wind (shear) which may impact aircraft lift. This complements a C-band weather radar, and an anemometer-based low-level shear warning system based on a locally installed network of detectors. The lidar is placed close to the HKIA runways so that the simple radial velocity can be used to estimate headwind. Verification against anemometer, SODAR and onboard QAR flight data performs quite well. LIWAS acts by algorithmically detecting headwind "ramps" and reporting them in order of a measure of severity, with an effective threshold of 15 kt for significant headwind changes over the ramp. LIWAS and the other warning sources are fed to approaching aircraft via air traffic control. Accounting for subjectivity in pilot reporting, and differences between the character of different ramps, warnings and reports were in general agreement. Wu and Hon (2018) term the above technique the glide path scan windshear alerting algorithm (GLYGA). They attempt to optimise the system by performing spectral decomposition of the headwind profiles. An algorithm applying thresholds to a given Fourier mode within the spectrum to warn of shear is applied; a given shear ramp will show up in a Fourier mode whose wavelength corresponds to the size of the ramp. While no individual Fourier mode outperforms GLYGA, combinations of channels with independently set thresholds mostly do marginally outperform GLYGA, when examined using ROC curves. Further improvements, for instance using Morlet wavelet analysis (as opposed to effectively sinusoidal Fourier decomposition), may make this comparison more decisive. Scanning doppler weather radar and scanning doppler lidar are also used in a windshear alerting system operating at

Las Vegas International Airport.

In a more integrated approach, Manninen et al. (2018) use vertically-pointing doppler lidar to characterise boundary layer turbulence in terms of EDR, shear and radial (i.e. vertical) velocity skewness in order to categorise different boundary layer conditions. A related categorisation of periods of differing mountain wave influence on boundary layer winds and turbulence (such as rotors) might be possible.

In order to account for deficiencies in turbulence spectra determined by scanning lidar compared to sonic anemometer-based spectra, Sathe and Mann (2012) apply a spectral tensor model to simulate spectra determined from lidar and sonic data under different conditions. The model takes into account beam angles, line-of-sight averaging, sampling rate, and the three-dimensional structure of the measured turbulence, and performs very well in explaining large differences between lidar- and sonic-based spectra.

8 Other remote sensing

A number of other sources of data are available to augment or complement measurements from locally installed doppler instruments. Satellite data are not subject to the same range limitations as surface based remote sensing. The use of high resolution (roughly 1 km) visible satellite images for detailed study of lee wave clouds is commonplace (e.g. Sheridan et al., 2007; Vosper et al., 2013). While not all locations are covered by geostationary satellites offering frequent, regular image updates, such as Meteosat Second Generation, or Himawari, various polar orbiting satellites with comparable or better resolution allow retrievals of images when the satellite passes overhead, such as the POES and MODIS instruments. Images from infrared instruments on the same satellite can be used to discern cloud top temperature and hence height.

Another, arguably underused, form of imaging from polar orbiting satellites is the use of Synthetic Aperture Radar (SAR) to determine winds over sea. This involves processing of radar backscatter from small (several centimetre-sized) waves on the sea surface (a form of Bragg scattering), at different points in the orbit, to obtain measurements of radar backscatter at very small scales (100s of metres). From SAR, a range of measurements can be derived over land and sea; of interest here is the derivation of wind speed information over sea. The backscatter over sea depends on the viewing parameters of the satellite, the wind speed, and the wind direction. Thus using estimates of wind direction from a weather model, or discerned from shear streaks in the backscatter image, wind speed may be determined using an empirical “geophysical model function” (GMF) for the scattering process. Unlike standard scatterometer wind products (such as QuikSCAT), these data can be obtained at very high resolution, with GMFs valid in theory down to $O(100\text{ m})$ scales, and very close to shore, so that the technique is of particular value in coastal or maritime locations to look at small-scale wind variability. A selection of satellites obtain these data, but for many locations overpasses in the appropriate scanning mode may be infrequent (the Sentinel-1 system overpasses

coastal areas of the UK roughly every 12 hours, with a revisit time at precisely the same location occurring only every 6 days; this would count as “frequent”).

Horstmann and Koch (2005) compare the results of different GMFs with winds from NWP models as a form of broad verification. They also apply a “local gradient” method, whereby wind streaks, which align with the wind direction, are characterised using the gradient of backscatter within the image. The resulting orientation determined for the streaks corresponds to the wind direction. Wind shadowing close to coasts can be used to remove the remaining direction ambiguity (or Shao et al., 2019, use scatterometer winds). The masking of sea ice (which introduces non-wind-directed linear structure in the image) is also necessary in cold locations. Ultimately in this way a fully independent determination of the horizontal vector wind field is possible. Other methods to determine wind direction can be applied, such as the wavelet analysis performed on SAR backscatter images by Zecchetto (2018), who look at data from multiple different agencies’ satellites: ENVISAT (now defunct), COSMO-SkyMed (now succeeded by COSMO-SkyMed SG), RADARSAT-2 (defunct, to be succeeded by RADARSAT Constellation), and Sentinel-1A,B. Mouche et al. (2012), meanwhile, discuss how wind direction can be inferred from offsets in the SAR doppler centroid, indicating that this would become easier with data from the then-upcoming Sentinel-1 instruments. A summary diagram of current and recent spaceborne SAR instruments and the radar bands in which they operate is presently available on the UNAVCO website, and further instruments exist (such as the Gaofen-3 satellite, Shao et al., 2019). Despite advances in retrieval algorithms, SAR wind data can be subject to errors in some conditions; Zecchetto (2018) compare NWP model, scatterometer and SAR surface wind fields, showing a case where the three disagree in speed and direction. Also, different GMFs which are commonly used can yield significantly different wind magnitudes, especially in high winds (Beal et al., 2005). Clearly supporting wind information (such as coastal stations, ship observations, or bouys) is desirable.

Numerous case studies have been highlighted using SAR. Beal et al. (2005) give a comprehensive overview of applications of SAR for studying marine wind patterns, including lee waves, gap jets and island wakes, as well as gust fronts, shear lines and other small-scale phenomena. Concerning topographic effects, Alpers et al. (2009) show examples of SAR winds from the Adriatic Bora, a common cause of wind damage and hazard in the mountainous Croatian coastal area, related to gap winds and low-level wave breaking; the SAR winds illustrate the influence of lee waves and surface jets from the Dinaric Alps. Alpers et al. (2011) show an example of Foehn over the Black Sea originating from the Caucasus, which encounters a cyclonic eddy, while Alpers et al. (2010) show lee waves and jets associated with another “Bora”-termed wind over the Black Sea, as well as weaker katabatic wind outflows. The latter studies use data from ENVISAT. Li et al. (2011) show a lee wave example over the coastal South China Sea, determining marine winds using ENVISAT data. Li et al. (2011, 2013); Miglietta et al. (2013) all use SAR winds to validate high-resolution model simulations of lee waves.

Other techniques involving novel use of satellite swath data include MODIS water vapour im-

agery (6.7 μm wavelength), which is weighted towards the 550hPa level, and in which perturbations due to lee waves around this level can be visualised over land (Uhlenbrock et al., 2007). Alternatively, column water vapour images, derived from near-infrared (NIR) data (Lyapustin et al., 2014), or thermal infrared (Papandrea et al., 2019), can be used. These are sensitive to variations closer to the surface, and can be derived using the appropriate algorithms over land (e.g. from MODIS data, Lyapustin et al., 2014), or over sea (e.g. from ATSR-2/AATSR data, Papandrea et al., 2019), providing a vivid depiction of lee wave patterns. The above data are available online at 1 km resolution. While these proxies of lee wave motion may not have a simple correspondence with vertical velocity amplitudes, simulated satellite data for each of these sources from NWP models can be verified directly in comparison to each. Although overpass times of these polar instruments will not be frequent, the sourcing of data from a collection of instruments will improve temporal coverage.

Photography represents a very simple, passive form of remote sensing which can be very powerful where atmospheric flows become evident through their impact on cloud structures or dust lofting (Ralph et al., 1997; Grubisic and Lewis, 2004; Doyle and Durran, 2004). Timelapse “sky camera” imagery has been deployed in a number of field campaigns studying lee waves (e.g. Mobbs et al., 2005; Sheridan et al., 2007; Grubisic et al., 2008). Sheridan et al. (2007) combined this with measurements of cloud base height to determine the precise location of lee wave clouds and so relate the wave phase to acceleration and deceleration of the near-surface wind beneath wave crests and troughs during a rotor event. Romatschke et al. (2017) describe using stereoscopic photogrammetric analysis of images of rotor clouds obtained during T-REX from two cameras deployed for this purpose, adapting common 3-D point cloud techniques for use with clouds, where a lack of sharply defined features creates a challenge. The visible cloud surface can thus be mapped in 3-D space, and by analysing small cloud advecting fragments, motion vectors could be retrieved. The use of a fish-eye lens, such as by Luce et al. (2018), allows a potentially full-hemisphere view of cloud formations to be recorded, which could also be deployed as a multi-camera set-up.

Temperature and water vapour profiles from spaceborne remote sensing instruments are widely assimilated and have a considerable positive impact on the quality of NWP model analyses. Spaceborne radiometers (passive) measure brightness temperatures in different wavelength bands. For a standard atmosphere, the brightness temperature at a given wavelength is a weighted average of the temperature over the depth of the atmosphere. The dominance of the respective weighting functions in different layers of the atmosphere for different wavelengths (reflecting the concentration of the absorbing gas at a given height, the strength of absorption/emission at each wavelength, and absorption by the concentration of gas intervening a layer and the detector) allows the brightness temperatures retrieved to be inverted, using appropriate constraints, to obtain the temperature profile (World Meteorological Organization, 2014a). Water absorption channels can then be used to obtain a water vapour profile. Passive limb sounders use absorption of radiation from, for example the solar spectrum at sunset as viewed from the position of the satellite, to determine equivalent information with a relatively poor horizontal, but improved vertical resolution (World Meteorological

Organization, 2014a).

Active satellite sounding methods include radio occultation, which measures the refraction of signals from navigation satellites through the atmosphere in limb mode, allowing for sub-km temperature vertical resolution in the troposphere, and down to the surface. Spaceborne doppler lidar instruments, such as on the recently launched Aeolus satellite, are designed to profile winds. In the case of Aeolus, in polar orbit, preliminary data shows winds at 1 km vertical resolution, with global coverage at 200 km resolution during its orbit. Other methods of wind inference include techniques (employed for instance at the Met Office) to determine atmospheric motion from analysis of cloud motion in satellite images.

In addition to their assimilation in NWP models, gridded satellite profile products are routinely available online for many satellites, for instance on NOAA's Office of Satellite and Product Operations (OSPO) website, or EUMETSAT's Earth Observation Portal. Archives of soundings are available, for instance on the Centre for Environment Data Analysis (CEDA) catalogue. With an appropriate appreciation of the products' limitations, these could be used to provide profile information where no other source is available, for instance where upwind profiles are logistically too difficult to measure directly using radiosondes or ground-based remote sensing.

Ground-based or airborne microwave radiometers may be used for profiling of temperature and water vapour in a similar way to the above satellite-borne instruments. For instance, Rose et al. (2005) quote vertical resolution $O(100\text{ m})$ up to a few kilometres range for a ground-based instrument. While this may be sufficient for observing the influence of upwind profile on lee waves in conditions where lee wave trapping is the result of smooth vertical variation in temperature, it could prove somewhat crude, though still useful, in situations where temperature inversions strongly influence wave dynamics. Chan and Lee (2011) have also shown that radiometers possess some skill for low-level windshear alerting.

A Radio-Acoustic Sounding System (RASS) is another method for obtaining temperature profiles in the boundary layer, deployed for instance in the T-REX campaign (Cohn et al., 2011). Here, a SODAR is used to generate an acoustic pulse. This pulse travels vertically at the speed of sound and may be tracked using radio frequency pulses due to the fluctuation in refractive index that it creates. The sound speed depends on temperature and thus a temperature profile can be inferred from the vertical track, while SODAR yields winds (World Meteorological Organization, 2014b). Utilising SODAR, this technique suffers from the same limitations, such as increasingly limited range in stronger winds.

Mode Selective Enhanced Surveillance (Mode-S EHS) data represent a routine report sent from aircraft to air traffic management systems, containing the aircraft's speed, direction, altitude and Mach number, from which meteorological observations of temperature and horizontal wind can be derived. Mode-S Meteorological Routine Aircraft Reports (MRAR) represent the direct report, provided at a higher precision, which is processed to produce the Mode-S EHS report which most commonly is the information transmitted. These reports can be easily intercepted and decoded on

the ground at considerable range using relatively simple, low cost antenna instrumentation (Stone and Kitchen, 2016). Although in fact a form of *in situ*, as opposed to remote, sensing, Mode-S data resembles a remote sensing data source in terms of its continuous, volume coverage, and is much cheaper to harness than typical remote sensing techniques. Away from airfields, coverage is concentrated at cruise level, and is more sparse. Close to airfields, approach and take-off paths result in data availability at a continuous range of levels down to the surface, and reports are much more concentrated. Accuracy of Mode-S MRAR is greater than Mode-S EHS due to the reduced precision of the latter as a result of processing (Mirza et al., 2016; Oude Nijhuis et al., 2018). Stone and Pearce (2016) report accuracies of $\sim 2 \text{ ms}^{-1}$ for wind components and $\sim 3\text{K}$ for temperature derived from Mode-S EHS, although smaller errors were found in a subsequent study (Stone, 2017). The latter study also describes systematic differences between reports during ascent and descent, and depending on wind direction, and notes that different biases in the data apply for different aircraft, operators (and airports). While Mode-S data are currently largely harnessed for data assimilation (Stone and Kitchen, 2016; Oude Nijhuis et al., 2018), and despite the above issues, this information could be particularly useful in studying lower and mid-tropospheric flow when the study area is close to one or more airports, particularly as an augmentation of a more comprehensive suite of dedicated instrumentation. Steen et al. (2010) also discuss the use of Mode-S to support a recommended lidar/radar airport monitoring system.

9 Summary

Two techniques of remote sensing are principally considered in this review: scanning doppler lidar and scanning doppler radar, which are commonly used for studying atmospheric motion at relatively fine scales and ranges in the mesoscale. In mountain wave cases, involving stable conditions where large hydrometeors (i.e. rain) are largely absent, the radar bands most likely to be useful are the Ka- and W-bands, which are dominated by returns from cloud, yielding some clear air returns, while mountain waves are commonly accompanied by characteristic clouds shaped by the flow. There are also, meanwhile, X-band radar instruments which have been recently designed with an emphasis on delivering usable levels of clear air returns. Although typically having a shorter maximum range, lidar is well suited to low-level mountain wave applications, where air particularly in the boundary layer tends to be largely clear, so that cloud radar coverage may be patchy. Lidar's maximum range is also comparable to or larger than the wavelength of typical lee waves, and thus sufficient to characterise the local wave field in terms of wave-induced flow variability over one or more wave cycles. A doppler lidar is also typically a somewhat less expensive and lower power, more portable instrument than a radar.

In general Doppler lidar has a number of features which make it well suited to detect lee waves and their effects on low-level winds and turbulence:

-
- fine resolution (10s of metres)
 - short minimum range (10s of metres to 100s metres, depending on the instrument)
 - good returns in clear air (when aerosol concentration sufficient)
 - validates well against in-situ measurements
 - contamination of doppler velocities by precipitation fall speed (when present) is relatively weak
 - produces returns from precipitation and cloud base, providing some data even where aerosol concentration is weak

as well as some weaknesses:

- maximum range limited by atmospheric attenuation to around 10 km
- limited returns where concentration of aerosol is low
- attenuated significantly in precipitation
- attenuated rapidly in cloud

Doppler radar also has respective strengths:

- resolution of modern instruments is often fine (O(10 m))
- a fairly short minimum range (100 m)
- W- and Ka-band instruments (and certain X-band instruments) give some returns in clear air/from aerosol
- gives returns from precipitation
- good returns in cloud (principally W- and Ka-band)
- validates well against in-situ measurements

and weaknesses:

- weak(er) returns in clear air
- contamination of doppler velocities by precipitation fall speed
- Ka- and especially W-band attenuated by precipitation, reducing effective range in rainy conditions (S–X bands conversely more attenuated in cloud, less in precipitation)
- W-band strongly attenuated by atmospheric moisture (Ka less so), reducing effective range in moist conditions
- maximum range shortens with decreasing wavelength band (S > C > X > Ka > W)

- instruments tuned for clear air returns often have long minimum ranges (kilometres)
- relatively expensive
- larger and require more power than lidar (less portable), though the precise power requirement depends on the instrument, and relatively compact and effective models do exist
- aliasing at long range or with large radial velocities requires “unfolding” of the doppler retrievals, although algorithms to perform this are commonplace

From the above it can be seen that the two techniques are in a number of ways complementary. For instance lidar generally cannot operate in cloud, while Ka-band radar gives the best returns and data quality from returns within cloud; W- or Ka-band returns in a cloud-free boundary layer may be weak, whereas lidar returns from aerosol tend to be their best in this region. On the other hand the two techniques can be used to reinforce each other where both provide data, for instance to assess precipitation fall speed contamination of doppler velocities, since the sensitivity of each to this is different. One of each instrument would allow mutual verification of doppler velocity measurement where instruments are collocated, with dual-doppler operation possible where instruments are a sufficient distance apart.

Although, based on the weight of literature, Ka- and W-bands seem best suited to lee wave study using radar, technological developments are beginning to make this less clear cut, with clear-air returns also increasingly possible for radar in other bands, exploiting the advantages (e.g. long range, diminished attenuation due to precipitation or atmospheric moisture) of longer wavelength instruments. It will be worth monitoring technological development to augment the findings of this review in any future procurement exercises, as erstwhile limitations are surmounted.

Dual- or multiple-doppler configurations most commonly involve two or more of the same kind of instrument (radar only or lidar only), and increase the value of information retrieved by allowing the construction of wind vectors where the instrument ranges overlap, where a single instrument only gives the radial component of wind velocity. On the other hand, where coverage by two or more instruments of different types overlaps, dual- or multiple-doppler techniques can be applied in a similar way. Another, generally less expensive way of imparting some directional information to the picture yielded by doppler scanning is via supporting instrumentation, such as surface stations or profiling methods (e.g. radiosondes or wind profilers). Additionally, techniques adapted from data assimilation can be used to retrieve a wind vector field which is consistent with the radial velocity field obtained from a single scanning doppler instrument, either in a vertical or horizontal plane, using appropriate conservation and continuity assumptions. The results can be remarkably accurate, especially in a qualitative sense, giving a more visually intuitive image of the flow, making flow details such as vortices and shear zones obvious to the eye. A full conical doppler radar scan may take $O(30\text{ s})$, while this can be speeded up by confining angular coverage to a narrower range (or just one beam path). A multiple doppler scan, which may require repeated revisits, or if obtaining 3-D coverage, building of multiple scan elevations/orientations, may take minutes.

In parallel with vector retrieval, doppler scans can be used, again with appropriate assumptions where necessary, to map turbulence information such as eddy dissipation rate (EDR) at high resolution in the scan, either from raw radial velocities, or from processed wind vector data, via a number of methods.

A number of supporting techniques can be inexpensively exploited to give an equivalent style of higher-dimensional representation of the flow field to support or complement remote sensing. Various satellite products, from straightforward visible images of cloud showing ripples associated with lee wave activity, to more sophisticated retrievals such as wind over sea surface derived from Synthetic Aperture Radar (SAR) instruments, or infrared water vapour images in clear air. Satellite data will inevitably be available at a lower frequency than dedicated lidar or radar data. Common photography, especially in stereoscopic timelapse, can provide surprisingly rich information on atmospheric motion and dynamics, from the motion of clouds, although the greatest value comes from a meticulous attitude to metadata recording. Mode-S information intercepted from live, automated aircraft reports is another inexpensive means of obtaining distributed coverage of weather variables at high spatial resolution.

As a final comment, a number of key papers from this review can be highlighted. Some covering the application of remote sensing in stable mountain flow cases: Shun et al. (2003a); Shun and Chan (2008); Li and Chan (2016); Politovich et al. (2011); Kuhnlein et al. (2013); French et al. (2015); Strauss et al. (2015, 2016).

Others (with some repetition) cover the instrumentation of airfields: Shun et al. (2003a); Shun and Chan (2008); Li and Chan (2016); Politovich et al. (2011); Boilley and Mahfouf (2013); Keohan et al. (2006); Oude Nijhuis et al. (2018); Thobois et al. (2018); Steen et al. (2010).

Meanwhile, many papers highlight the benefit of combining multiple remote sensing instruments (of the same or different kinds): Fernando et al. (2019); Barthelmie and Pryor (2019); Drechsel et al. (2009); Hill et al. (2010); van Dooren et al. (2016).

Others cover comparisons between different types, demonstrating their complementarity: Traumer et al. (2008, 2009, 2010); Oude Nijhuis et al. (2018); Adler and Kalthoff (2016); Borque et al. (2016); Buhl et al. (2015); Steen et al. (2010).

References

- Adler, B., and N. Kalthoff, 2016: The impact of upstream flow on the atmospheric boundary layer in a valley on a mountainous island. *Boundary-Layer Meteorol.*, **158**, 429–452.
- Alpers, W., A. Y. Ivanov, and K.-F. Dagestad, 2009: Observations of Bora events over the Adriatic Sea and Black Sea by spaceborne Synthetic Aperture Radar. *Mon. Wea. Rev.*, **137**, 1150–1161.
- Alpers, W., A. Y. Ivanov, and K.-F. Dagestad, 2010: Investigation of coastal wind fields over the Black Sea using *Envisat*. *Proceedings of ESA Living Planet Symposium, 28 June - 2 July 2010*, Bergen, Norway, European Space Agency.
- Alpers, W., A. Y. Ivanov, and K.-F. Dagestad, 2011: Encounter of foehn wind with an atmospheric eddy over the Black Sea as observed by the Synthetic Aperture Radar onboard *Envisat*. *Mon. Wea. Rev.*, **139**, 3992–4000.
- Banakh, V. A., and I. N. Smalikho, 2016: Lidar observations of atmospheric internal waves in the boundary layer of the atmosphere on the coast of Lake Baikal. *Atmos. Meas. Tech.*, **9**, 5239–5248.
- Banakh, V. A., I. N. Smalikho, and A. V. Falits, 2017: Estimation of the turbulence energy dissipation rate in the atmospheric boundary layer from measurements of the radial wind velocity by micropulse coherent Doppler lidar. *Optics Express*, **25**, 22 679.
- BarbareSCO, F., L. Thobois, A. Dolfi-Bouteyre, N. Jeannin, R. Wilson, M. Valla, and A. Hallermeyer, 2015: Monitoring wind, turbulence and aircraft wake vortices by high resolution radar and lidar remote sensors in all weather conditions. in *Actes URSI France, Journ Scientifiques, March 2015*, 81–110.
- Barkwith, A., and C. G. Collier, 2011: Lidar observations of flow variability over complex terrain. *Meteorol. Appl.*, **18**, 372–382.
- Barthelmie, R. J., and S. C. Pryor, 2019: Automated wind turbine wake characterization in complex terrain. *Atmos. Meas. Tech. Discuss.*, submitted, doi:10.5194/amt-2018-461.
- Beal, R., G. Young, F. Monaldo, D. Thompson, N. Winstead, and C. Scott, 2005: High resolution wind monitoring with wide swath SAR: A user's guide. Tech. rep., U.S. Dept. of Commerce, National Oceanographic and Atmospheric Administration, National Environmental Satellite, Data and Information Service, and Office of Research and Applications, 164 pp.
- Bell, T., P. Klein, N. Wildmann, and R. Menke, 2019: Analysis of flow in complex terrain using multi-Doppler lidar retrievals. *Atmos. Meas. Tech. Discuss.*, submitted.
- Boilley, A., and J.-F. Mahfouf, 2013: Wind shear over the Nice Côte d'Azur airport: case studies. *Nat. Hazards Earth Syst. Sci.*, **13**, 2223–2238.

-
- Borque, P., E. Luke, and P. Kollias, 2016: On the unified estimation of turbulence eddy dissipation rate using Doppler cloud radars and lidars. *J. Geophys. Res. Atmos.*, **120**, 5972–5989.
- Bose, S., 2016: Application of scanning Doppler cloud radar in the atmospheric sounding of winds. Masters thesis, Department of Electrical and Electronics Engineering, Birla Institute of Technology, Mesra-835215, Ranchi, 65pp pp.
- Bouniol, D., A. J. Illingworth, and R. J. Hogan, 2003: Deriving turbulent kinetic energy dissipation rate within clouds using ground based 94 GHz radar. *31st Conf. on Radar Meteorology*, Seattle, WA, American Meteorological Society.
- Buhl, J., R. Leinweber, U. Gorsdorf, M. Radenz, A. Ansmann, and V. Lehmann, 2015: Combined vertical-velocity observations with Doppler lidar, cloud radar and wind profiler. *Atmos. Meas. Tech.*, **8**, 3527–3536.
- Chan, P. W., 2008: Measurement of turbulence intensity profile by a mini-sodar. *Meteorol. Appl.*, **15**, 249–258.
- Chan, P. W., and K. K. Hon, 2016: Observation and numerical simulation of terrain-induced wind-shear at the Hong Kong International Airport in a planetary boundary layer without temperature inversions. *Adv. Meteorol.*, 1454513.
- Chan, P. W., and Y. F. Lee, 2011: Application of a ground-based, multi-channel microwave radiometer to the alerting of low-level windshear at an airport. *Met. Zeit.*, **20**, 423–429.
- Chan, P. W., and M. W. Shao, 2007: Depiction of complex airflow near Hong Kong International Airport using a Doppler LIDAR with a two-dimensional wind retrieval technique. *Met. Zeit.*, **16**, 491–504.
- Choukulkar, A., R. Calhoun, B. Billings, and J. Doyle, 2012: Investigation of a complex nocturnal flow in Owens Valley, California using coherent Doppler lidar. *Boundary-Layer Meteorol.*, **144**, 359–378.
- Choukulkar, A., and Coauthors, 2017: Evaluation of single and multiple Doppler lidar techniques to measure complex flow during the XPIA field campaign. *Atmos. Meas. Tech.*, **10**, 247–264.
- Chouza, F., O. Reitebuch, M. Jahn, S. Rahm, and B. Weinzierl, 2016: Vertical wind retrieved by airborne lidar and analysis of island induced gravity waves in combination with numerical models and in situ particle measurements. *Atmos. Chem. Phys.*, **16**, 4675–4692.
- Cohn, S. A., V. Grubisic, and W. O. J. Brown, 2011: Wind profiler observations of mountain waves and rotors during T-REX. *J. Appl. Meteor. Climatol.*, **50**, 826–843.
- Debnath, M., and Coauthors, 2017: Assessment of virtual towers performed with scanning wind lidars and Ka-band radars during the XPIA experiment. *Atmos. Meas. Tech.*, **10**, 1215–1227.

- Devara, P. C. S., Y. J. Rao, S. M. Sonbawne, M. G. Manoj, K. K. Dani, and S. K. Saha, 2015: First results of compact coherent Doppler wind lidar and its validation at IITM, Pune, India. *Meteorol. Appl.*, **22**, 156–164.
- Doyle, J. D., and D. R. Durran, 2004: Recent developments in the theory of atmospheric rotors. *Bull. Amer. Meteor. Soc.*, **85**, 337–342.
- Drechsel, S., M. Chong, G. J. Mayr, M. Weissmann, R. Calhoun, and A. Dornbrack, 2009: Three-dimensional wind retrieval: Application of MUSCAT to dual-Doppler lidar. *J. Appl. Meteor. Climatol.*, **26**, 635–646.
- Ducrocq, V., and Coauthors, 2014: HyMeX-SOP1: The field campaign dedicated to heavy precipitation and flash flooding in the northwestern Mediterranean. *Bull. Amer. Meteor. Soc.*, **95** (7), 1083–1100, doi:10.1175/BAMS-D-12-00244.1.
- Fernando, H. J. S., and Coauthors, 2019: The Perdigao: Peering into microscale details of mountain winds. *Bull. Amer. Meteor. Soc.*, *in press*.
- French, J. R., S. Haimov, L. Oolman, V. Grubisic, S. Serafin, and L. Strauss, 2015: Wave-induced boundary layer separation in the lee of the Medicine Bow mountains. part i: Observations. *J. Atmos. Sci.*, **72**, 4845–4863.
- Grubisic, V., and J. M. Lewis, 2004: Sierra Wave Project revisited: 50 years later. *Bull. Amer. Meteor. Soc.*, **85**, 1127–1142.
- Grubisic, V., and Coauthors, 2008: The Terrain-Induced Rotor Experiment: a field campaign overview including observational highlights. *Bull. Amer. Meteor. Soc.*, **89**, 1513–1533.
- Grund, C. J., R. M. Banta, J. L. George, J. N. Howell, M. J. Post, R. A. Richter, and A. M. Weickmann, 2001: High-resolution Doppler lidar for boundary layer and cloud research. *J. Atmos. Oceanic Technol.*, **18**, 376–393.
- Gunter, W. S., J. L. Schroeder, and B. D. Hirth, 2015: Validation of dual-Doppler wind profiles with in situ anemometry. *J. Atmos. Oceanic Technol.*, **32**, 943–960.
- Hill, M., R. Calhoun, H. Fernando, A. Wieser, A. Dornbrack, M. Weissmann, G. Mayr, and R. Newsom, 2010: Coplanar Doppler lidar retrieval of rotors from T-REX. *J. Atmos. Sci.*, **67**, 713–729.
- Hirth, B. D., J. L. Schroeder, and J. G. Guynes, 2017: Diurnal evolution of wind structure and data availability measured by the DOE prototype radar system. *IOP Conf. Series: Journal of Physics: Conf. Series*, **926**, 012 003.
- Hogan, R. J., N. Gaussiat, and A. J. Illingworth, 2005: Stratocumulus liquid water content from dual-wavelength radar. *J. Atmos. Oceanic Technol.*, **22**, 1207–1218.

- Hon, K. K., and P. W. Chan, 2013: Application of LIDAR-derived eddy dissipation rate profiles in low-level wind shear and turbulence alerts at Hong Kong International Airport. *Meteorol. Appl.*, **21**, 74–85.
- Hon, K. K., and P. W. Chan, 2014: Terrain-induced turbulence intensity during tropical cyclone passage as determined from airborne, ground-based, and remote sensing sources. *J. Atmos. Oceanic Technol.*, **31**, 2373–2391.
- Horstmann, J., and W. Koch, 2005: Measurement of ocean surface winds using synthetic aperture radars. *IEEE J. Ocean. Eng.*, **30**, 508–515.
- Howard Jr., A. Q., and T. Naini, 2012: Four methods for LIDAR retrieval of microscale wind fields. *Remote Sens.*, **4**, 2329–2355.
- ICAO, 2001: Meteorological service for international air navigation. annex 3 to the Convention on International Civil Aviation, 14th Ed. Icao rep., International Civil Aviation Organization, 128 pp.
- Kadygrov, E. N., 2005: INTEGRATED PROFILING SYSTEMS AND OTHER UPPER-AIR MEASUREMENT TECHNIQUES: Operational aspects of different ground-based remote sensing observing techniques for vertical profiling of temperature, wind, humidity and cloud structure. Expert team on remote sensing upper-air technology and techniques, CIMO/OPAG-UPPER-AIR/ET-RSUAT&T-1/Doc.6.2(1), WORLD METEOROLOGICAL ORGANIZATION, 41 pp.
- Keohan, C. F., K. Barr, and S. M. Hannon, 2006: Evaluation of pulsed lidar wind hazard detection at Las Vegas International Airport. P5.4, *12th Conference on Aviation Range and Aerospace Meteorology*, Atlanta, GA, American Meteorological Society.
- Koch, G. J., M. J. Kavaya, B. W. Barnes, J. Y. Beyon, M. Petros, J. Yu, F. Amzajerjian, and U. N. Singh, 2006: P5.5 wind measurements with high-energy doppler lidar. *12th Conference on Aviation Range and Aerospace Meteorology, during 86th American Meteorological Society Annual Meeting*, Atlanta, GA, American Meteorological Society.
- Koch, S. E., C. Flamant, J. W. Wilson, B. M. Gentry, and B. D. Jamison, 2008: An atmospheric soliton observed with Doppler radar, differential absorption lidar, and a molecular Doppler lidar. *J. Atmos. Oceanic Technol.*, **25**, 1267–1287.
- Kollias, P., N. Bharadwaj, K. Widener, I. Jo, and K. Johnson, 2014a: Scanning ARM cloud radars. part i: Operational sampling strategies. *J. Atmos. Oceanic Technol.*, **31**, 569–582.
- Kollias, P., I. Jo, P. Borque, A. Tatarevic, K. Lamer, N. Bharadwaj, K. Widener, and E. E. Clothiaux, 2014b: Scanning ARM cloud radars. part ii: Data quality control and processing. *J. Atmos. Oceanic Technol.*, **31**, 583–598.
- Krishnamurthy, R., R. Calhoun, B. Billings, and J. Doyle, 2011: Wind turbulence estimates in a valley by coherent Doppler lidar. *Meteorol. Appl.*, **18**, 361–371.

- Kuhnlein, C., A. Dornbrack, and M. Weissmann, 2013: High-resolution Doppler lidar observations of transient downslope flows and rotors. *Mon. Wea. Rev.*, **141**, 3257–3272.
- Lawson, J., G. Vaughan, and M. S. D, 2011: Classifying fronts in data from a VHF wind-profiling radar. *Atmos. Sci. Lett.*, **12**, 375–380.
- Li, L., and P. W. Chan, 2016: LIDAR observation and numerical simulation of vortex/wave shedding at the Eastern Runway Corridor of the Hong Kong International Airport. *Meteorol. Appl.*, **23**, 379–388.
- Li, X., W. Zheng, X. Yang, iJ. A. Zhang, W. G. Pichel, and Z. Li, 2013: Coexistence of atmospheric gravity waves and boundary layer rolls observed by SAR. *J. Atmos. Sci.*, **70**, 3448–3459.
- Li, X., W. Zheng, X. Yang, Z. Li, and W. G. Pichel, 2011: Sea surface imprints of coastal mountain lee waves imaged by synthetic aperture radar. *J. Geophys. Res.: Atmospheres*, **116**, C02014.
- Lottman, B. T., R. G. Frehlich, S. M. Hannon, and S. W. Henderson, 2001: Evaluation of vertical winds near and inside a cloud deck using coherent Doppler lidar. *J. Atmos. Oceanic Technol.*, **18**, 1377–1386.
- Luce, H., L. Kantha, M. Yabuki, and H. Hashiguchi, 2018: Atmospheric Kelvin-Helmholtz billows captured by the MU radar, lidars and a fish-eye camera. *Earth, Planets and Space*, **70**, 162.
- Lundquist, J. K., and Coauthors, 2017: Assessing state-of-the-art capabilities for probing the atmospheric boundary layer: The XPIA field campaign. *Bull. Amer. Meteor. Soc.*, **98**, 289–314.
- Lyapustin, A., M. J. Alexander, L. Ott, A. Molod, B. Holben, J. Susskind, and Y. Wang, 2014: Observation of mountain lee waves with MODIS NIR column water vapor. *Geophys. Res. Lett.*, **41**, 710–716.
- Mann, J., R. Menke, N. Vasiljevic, J. Berg, and N. Troldborg, 2018: Challenges in using scanning lidars to estimate wind resources in complex terrain. *J. Phys.: Conf. Ser.*, **1037**, 072017.
- Manninen, A. J., T. Marke, M. J. Tuononen, and E. J. O'Connor, 2018: Atmospheric boundary layer classification with Doppler lidar. *J. Geophys. Res.: Atmospheres*, **123**, 8172–8189.
- Matrosov, S. Y., D. E. Kingsmill, B. E. Martner, and F. M. Ralph, 2005: The utility of X-band polarimetric radar for quantitative estimates of rainfall parameters. *J. Hydrometeorol.*, **6**, 248–262.
- Medina, S., and R. A. Houze Jr., 2016: Kelvin-Helmholtz waves in extratropical cyclones passing over mountain ranges. *Q. J. R. Meteorol. Soc.*, **142**, 1311–1319.
- Menke, R., N. Vasiljevic, K. S. Hansen, A. N. Hahmann¹, and J. Mann, 2018: Does the wind turbine wake follow the topography? a multi-lidar study in complex terrain. *Wind Energ. Sci.*, **3**, 681–691.

- Menke, R., N. Vasiljevic, J. Mann, and J. K. Lundquist, 2019: Characterization of flow recirculation zones in complex terrain using multi-lidar measurements. *Atmos. Chem. Phys. Discuss.*, under review.
- Miglietta, M. M., S. Zecchetto, and F. De Biasio, 2013: A comparison of WRF model simulations with SAR wind data in two case studies of orographic lee waves over the Eastern Mediterranean Sea. *Atmos. Res.*, **120–121**, 127–146.
- Mirza, A. K., S. P. Ballard, S. L. Dance, P. Maisey, G. G. Rooney, and E. K. Stone, 2016: Comparison of aircraft-derived observations with *in situ* research aircraft measurements. *Q. J. R. Meteorol. Soc.*, **142**, 2949–2967.
- Mobbs, S. D., and Coauthors, 2005: Observations of downslope winds and rotors in the Falkland Islands. *Q. J. R. Meteorol. Soc.*, **131**, 329–351.
- Moran, K. P., B. E. Martner, M. J. Post, R. A. Kropfli, D. C. Welsh, and K. B. Widener, 1998: An unattended cloud-profiling radar for use in climate research. *Bull. Amer. Meteor. Soc.*, **79**, 443–455.
- Mouche, A. A., F. Collard, B. Chapron, K.-F. Dagestad, G. Guitton, J. A. Johannessen, V. Kerbaol, and M. W. Hansen, 2012: On the use of Doppler shift for sea surface wind retrieval from SAR. *IEEE Trans. Geosci. Remote Sens.*, **50**, 2901–2909.
- Nygaard, N. G., and C. Newcombe, 2018: Wake behind an offshore wind farm observed with dual-Doppler radars. *J. Phys.: Conf. Ser.*, **1037**, 072 008.
- O'Connor, E. J., R. J. Hogan, and A. J. Illingworth, 2005: Retrieving stratocumulus drizzle parameters using Doppler radar and lidar. *J. Appl. Meteorol.*, **44**, 14–27.
- O'Connor, E. J., A. J. Illingworth, I. M. Brooks, C. D. Westbrook, R. J. Hogan, F. Davies, and B. J. Brooks, 2010: A method for estimating the turbulent kinetic energy dissipation rate from a vertically pointing Doppler lidar, and independent evaluation from balloon-borne *in situ* measurements. *J. Atmos. Oceanic Technol.*, **27**, 1652–1664.
- Oude Nijhuis, A. C. P., and Coauthors, 2018: Wind hazard and turbulence monitoring at airports with lidar, radar, and Mode-S downlinks: The UFO Project. *Bull. Amer. Meteor. Soc.*, **99**, 2275–2293.
- Papandrea, E., S. Casadio, E. Castelli, B. M. Dinelli, and M. M. Miglietta, 2019: Lee waves detection over the Mediterranean Sea using the Advanced Infra-Red WAter Vapour Estimator (AIRWAVE) total column water vapor (TCWV) dataset. *Atmos. Meas. Tech. Discuss.*, *in review*.
- Paschke, E., R. Leinweber, and V. Lehmann, 2015: Doppler lidar for operational vertical wind profiling based on a 1-year trial. *Atmos. Meas. Tech.*, **8**, 2251–2266.
- Pauscher, L., and Coauthors, 2016: An inter-comparison study of multi- and DBS Lidar measurements in complex terrain. *Remote Sens.*, **8**, 782.

- Pokharel, B., B. Geerts, X. Chu, and P. Bergmaier, 2017: Profiling radar observations and numerical simulations of a downslope wind storm and rotor on the lee of the Medicine Bow Mountains in Wyoming. *Atmosphere*, **8**, 39.
- Politovich, M. K., R. K. Goodrich, C. S. Morse, A. Yates, R. Barron, and S. A. Cohn, 2011: The Juneau terrain-induced turbulence alert system. *Bull. Amer. Meteor. Soc.*, **92**, 299–313.
- Qiu, C.-J., A.-M. Shao, S. Liu, and Q. Xu, 2006: A two-step variational method for three-dimensional wind retrieval from single Doppler radar. *Meteorol. Atmos. Phys.*, **91**, 1–8.
- Ralph, F. M., and P. J. Neiman, 1997: Lidar observations of a breaking mountain associated with extreme turbulence. *Geophys. Res. Letts.*, **24**, 663–666.
- Ralph, F. M., P. J. Neiman, T. L. Keller, D. Levinson, and L. Fedor, 1997: Observations, simulations, and analysis of nonstationary trapped lee waves. *Mon. Wea. Rev.*, **54**, 1308–1333.
- Romatschke, U., V. Grubisic, and J. A. Zehnder, 2017: Photogrammetric analysis of rotor clouds observed during T-REX. *Poster 443, 97th American Meteorological Society Annual Meeting*, Seattle, WA, American Meteorological Society.
- Rose, T., S. Crewell, U. Lohnert, and C. Simmer, 2005: A network suitable microwave radiometer for operational monitoring of the cloudy atmosphere. *Atmos. Res.*, **75**, 183–200.
- Sathe, A., and J. Mann, 2012: Measurement of turbulence spectra using scanning pulsed wind lidars. *J. Geophys. Res.*, **117**, D01 201.
- Shao, W., S. Zhu, J. Sun, X. Yuan, Y. Sheng, Q. Zhang, and Q. Ji, 2019: Evaluation of wind retrieval from co-polarization Gaofen-3 SAR imagery around China seas. *J. Ocean Univ. China*, **18**, 80–92.
- Sharman, R. D., L. B. Cornman, G. Meymaris, J. Pearson, and T. Farrar, 2014: Description and derived climatologies of automated in situ eddy-dissipation-rate reports of atmospheric turbulence. *J. Appl. Meteor. Climatol.*, **53**, 1416–1432.
- Sharman, R. D., and J. M. Pearson, 2017: Prediction of energy dissipation rates for aviation turbulence. part I: Forecasting nonconvective turbulence. *J. Appl. Meteor. Climatol.*, **56**, 317–337.
- Sheridan, P. F., V. Horlacher, G. G. Rooney, P. Hignett, S. D. Mobbs, and S. B. Vosper, 2007: Influence of lee waves on the near-surface flow downwind of the Pennines. *Q. J. R. Meteorol. Soc.*, **133**, 1353–1369.
- Shun, C. M., and P. W. Chan, 2008: Applications of an infrared Doppler lidar in detection of wind shear. *J. Atmos. Oceanic Technol.*, **25**, 637–655.
- Shun, C. M., C. M. Cheng, and O. S. M. Lee, 2003a: Reprint 509: LIDAR observations of terrain-induced flow and its application in airport wind shear monitoring. *International Conference on Alpine*

-
- Meteorology (ICAM) and Mesoscale Alpine Programme (MAP) Meeting, 19-23 May 2003, Brig, Switzerland, International Conference on Alpine Meteorology (ICAM).*
- Shun, C. M., S. Y. Lau, and O. S. M. Lee, 2003b: Terminal Doppler weather radar observation of atmospheric flow over complex terrain during tropical cyclone passages. *J. Appl. Meteorol.*, **42**, 1697–1710.
- Steen, M., S. Schonhals, J. Polvinen, P. Drake, J.-P. Cariou, A. Dolfi-Bouteyre, and F. Barbaresco, 2010: Candidate technologies survey of airport wind & wake-vortex monitoring sensors. *Sensors for Weather & Wake-Vortex Hazards Mitigation, 9th Innovative Research Workshop & Exhibition, Bretigny-sur-Orge, France, The European Organisation for Safety of Air Navigation (Eurocontrol).*
- Stone, E. K., 2017: A comparison of Mode-S Enhanced Surveillance observations with other in situ aircraft observations. *Q. J. R. Meteorol. Soc.*, **144**, 695–700.
- Stone, E. K., and M. Kitchen, 2016: Deriving meteorological observations from intercepted Mode-S EHS messages. *Poster P2(65), WMO Technical Conference on Meteorological and Environmental Instruments and Methods of Observation (CIMO TECO 2016), Madrid, Spain, World Meteorological Organisation.*
- Stone, E. K., and G. Pearce, 2016: A network of Mode-S receivers for routine acquisition of aircraft-derived meteorological data. *J. Atmos. Oceanic Technol.*, **33**, 757–768.
- Strauss, L., S. Serafin, and V. Grubisic, 2016: Atmospheric rotors and severe turbulence in a long deep valley. *J. Atmos. Sci.*, **73**, 1481–1506.
- Strauss, L., S. Serafin, S. Haimov, and V. Grubisic, 2015: Turbulence in breaking mountain waves and atmospheric rotors estimated from airborne in situ and Doppler radar measurements. *Q. J. R. Meteorol. Soc.*, **141**, 3207–3225.
- Tang, W., P. W. Chan, and G. Haller, 2011: Lagrangian coherent structure analysis of terminal winds detected by lidar. part II: Structure evolution and comparison with flight data. *J. Appl. Meteor. Climatol.*, **50**, 2167–2183.
- Thobois, L., J.-P. Cariou, and I. Gultepe, 2018: Review of Lidar-Based Applications for Aviation Weather. *Pure Appl. Geophys.*, **176**, 1959–1976.
- Traumner, K., J. Handwerker, A. Wieser, and J. Grenzhauer, 2008: Simultaneous wind measurements with lidar and cloud radar: Complementarity and quality check. *Proceedings of the Fifth European Conference on Radar in Meteorology and Hydrology, Helsinki, Finland.*
- Traumner, K., J. Handwerker, A. Wieser, and J. Grenzhauer, 2010: A synergy approach to estimate properties of raindrop size distributions using a Doppler lidar and cloud radar. *J. Atmos. Oceanic Technol.*, **27**, 1095–1100.

- Traumner, K., J. Handwerker, A. Wieser, J. Grenzhäuser, and C. Kottmeier, 2009: Advantages of a coordinated scanning Doppler lidar and cloud radar system for wind measurements. *89th American Meteorological Society Annual Meeting*, Phoenix, AZ, American Meteorological Society.
- Udina, M., M. R. Soler, and O. Sol, 2017: A modeling study of a trapped lee-wave event over the Pyrenees. *Mon. Wea. Rev.*, **145**, 75–96.
- Uhlenbrock, N. L., K. M. Bedka, W. F. Feltz, and S. A. Ackerman, 2007: Mountain wave signatures in MODIS 6.7- μm imagery and their relation to pilot reports of turbulence. *Weather Forecast.*, **22**, 662–670.
- Valenzuela, R. A., and D. E. Kingsmill, 2017: Terrain-trapped airflows and orographic rainfall along the coast of northern California. part I: Kinematic characterization using a wind profiling radar. *Mon. Wea. Rev.*, **145**, 2993–3008.
- Valenzuela, R. A., and D. E. Kingsmill, 2018: Terrain-trapped airflows and orographic rainfall along the coast of northern California. part II: Horizontal and vertical structures observed by a scanning Doppler radar. *Mon. Wea. Rev.*, **146**, 2381–2402.
- Valdecabres, L., N. G. Nygaard, L. Vera-Tudela, L. von Bremen, and M. Kuhn, 2018: On the use of dual-Doppler radar measurements for very short-term wind power forecasts. *Remote Sens.*, **10**, 1701.
- van Dooren, M. F., D. Trabucchi, and M. Kuhn, 2016: A methodology for the reconstruction of 2D horizontal wind fields of wind turbine wakes based on dual-Doppler lidar measurements. *Remote Sens.*, **8**, 809.
- Vasiljevic, N., and Coauthors, 2017: Perdigao 2015: methodology for atmospheric multi-Doppler lidar experiments. *Atmos. Meas. Tech.*, **10**, 3463–3483.
- Vosper, S. B., H. Wells, J. A. Sinclair, and P. F. Sheridan, 2013: A climatology of lee waves over the UK derived from model forecasts. *Meteorol. Appl.*, **20**, 466–481.
- Vosper, S. B., and R. M. Worthington, 2002: VHF radar measurements and model simulations of mountain waves over Wales. *Q. J. R. Meteorol. Soc.*, **128**, 185–204.
- Wang, Y., C. M. Hocutt, S. W. Hoch, E. Creegan, H. J. S. Fernando, C. D. Whiteman, M. Felton, and G. Huynh, 2016: Triple Doppler wind lidar observations during the mountain terrain atmospheric modeling and observations field campaign. *J. Appl. Remote Sens.*, **10**, 026 015.
- Weiss, C. C., J. L. Schroeder, J. Guynes, P. Skinner, and J. Beck, 2009: The TTUKa mobile Doppler radar: Coordinated radar and in situ measurements of supercell thunderstorms during project VORTEX2. *11B.2, 34th Conference on Radar Meteorology*, Williamsburg, VA, USA, American Meteorological Society.

-
- Weissmann, M., A. Dornbrack, and J. D. Doyle, 2009: Vorticity from line-of-sight lidar velocity scans. *J. Atmos. Oceanic Technol.*, **26**, 2683–2690.
- Witschas, B., S. Rahm, A. Dornbrack, J. Wagner, and M. Rapp, 2017: Airborne wind lidar measurements of vertical and horizontal winds for the investigation of orographically induced gravity waves. *J. Atmos. Oceanic Technol.*, **34**, 1371–1386.
- World Meteorological Organization, 2014a: Principles of Earth observation from space. *Guide to Meteorological Instruments and Methods of Observation (the CIMO Guide) 2014 edition, Part II, Chapter 2*, World Meteorological Organization, Geneva, Switzerland, 46pp.
- World Meteorological Organization, 2014b: Special profiling techniques for the boundary layer and the troposphere. *Guide to Meteorological Instruments and Methods of Observation (the CIMO Guide) 2014 edition, Part II, Chapter 5*, World Meteorological Organization, Geneva, Switzerland, 54pp.
- Worthington, R. M., 1998: Tropopausal turbulence caused by the breaking of mountain waves. *J. Atmospheric Sol.-Terr. Phys.*, **60**, 1543–1547.
- Worthington, R. M., 2004: All-weather volume imaging of the boundary layer and troposphere using the MU radar. *Annales Geophysicae*, **22**, 1407–1419.
- Worthington, R. M., 2005: VHF volume-imaging radar observation of aspect-sensitive scatterers tilted in mountain waves above a convective boundary layer. *Annales Geophysicae*, **23**, 1139–1145.
- Wu, T.-C., and K. K. Hon, 2018: Application of spectral decomposition of LIDAR-based headwind profiles in windshear detection at the Hong Kong International Airport. *Met. Zeit.*, **27**, 33–42.
- Wurman, J., J. Straka, E. Rasmussen, M. Randall, and A. Zahrai, 1997: Design and deployment of a portable, pencil-beam, pulsed, 3-cm Doppler radar. *J. Atmos. Oceanic Technol.*, **14**, 1502–1512.
- Zecchetto, S., 2018: Wind direction extraction from SAR in coastal areas. *Remote Sens.*, **10**, 261.

Met Office

FitzRoy Road, Exeter
Devon, EX1 3PB
UK

Tel: 0370 900 0100

Fax: 0370 900 5050

enquiries@metoffice.gov.uk

www.metoffice.gov.uk